TITLE

1D ELASTIC FULL-WAVEFORM INVERSION AND UNCERTAINTY ESTIMATION BY MEANS OF A HYBRID GENETIC ALGORITHM-GIBBS SAMPLER APPROACH

Aleardi Mattia, Mazzotti Alfredo

University of Pisa, Earth Sciences Department

Via S. Maria 53, 56126, Pisa (Italy)

mattia.aleardi@dst.unipi.it

ABSTRACT

Stochastic optimization methods such as Genetic Algorithms (GA's) search for the global minimum of the misfit function within a given parameter range and do not require any calculation of the gradients of the misfit surfaces. More importantly, these methods collect a series of models and associated likelihoods that can be used to estimate the posterior probability distribution (PPD). However, because GA's are not a Markov Chain Monte Carlo method (MCMC), the direct use of the GA-sampled models and their associated likelihoods produce a biased estimation of the PPD. In contrast, MCMC methods, such as the Metropolis-Hastings and Gibbs sampler, provide accurate PPDs but at considerable computational cost. In this work, we use a hybrid method that combines the speed of GA to find an optimal solution and the accuracy of a Gibbs Sampler (GS) to obtain a reliable estimation of the posterior probability distributions. First, we test this method on an analytical function and show that the GA method cannot recover the true probability distributions and that it tends to underestimate the true uncertainties. Conversely, combining the GA optimization with a GS step enables us to recover the true PPD. Then, we demonstrate the applicability of this hybrid method by performing 1D elastic Full-Waveform Inversions (FWI) on synthetic and field data. We also discuss how an appropriate GA implementation is essential to attenuate the "genetic drift" effect and to maximize the exploration of the model space. In fact, a wide and efficient exploration of the model space is important not only to avoid entrapment in local minima during the GA optimization but also to ensure a reliable estimation of the posterior probability distribution in the subsequent GS step.

KEYWORDS

Full-waveform inversion, Elastic, Stochastic.

33

Introduction

Full-waveform inversion (FWI) is a data-fitting procedure that is based on full-wavefield modelling to extract quantitative information from seismograms (Tarantola, 1986). The aim is to exploit the full information content of the data to derive high-resolution quantitative models of the subsurface. Most recent developments have focused on building P-wave velocity models to be used as improved background velocity fields for wave equation depth migration (Vireux and Operto, 2009; Sirgue et al. 2010; Prieux et al. 2011; Morgan et al. 2013). In this context, the FWI is usually solved in the acoustic approximation and by applying gradient-based methods (such as the Gauss-Newton or conjugate gradient). A limitation of the gradient-based methods is their local nature and the consequent requirement of a good starting model to avoid convergence toward local minima. A way to overcome this problem is to use stochastic optimization methods, which are less affected by the presence of local minima in the misfit function but require huge computational efforts.

Stochastic FWI was first performed in the 1990s to invert single-shot gathers, assuming an acoustic approximation and 1D geological models. In this context, the limited number of model parameters made it possible to apply global optimization techniques, such as simulated annealing and genetic algorithms (Sen and Stoffa, 1991; 1992). For many practical applications, the stochastic approach to elastic FWI is usually limited to horizontally stratified media using reflectivity method (Mallick, 1999; Mallick and Dutta 2002; Mallick et al. 2010; Fliedner et al. 2012; Li and Mallick, 2015). It is known that the computational cost of stochastic methods grows exponentially with the number of unknowns. Such scaling problem is sometimes referred to as the "curse of dimensionality" (Bellman, 1957) and it makes the stochastic, elastic, FWI unfeasible for 2D or 3D applications in which thousands or even millions of unknowns are considered. However, thanks to the recent growth of high performance computing, the stochastic approach to FWI begins to be used to derive accurate, low-resolution, 2D or 3D compressional velocity fields that are well-suited to play the role of starting models for gradient-based, acoustic, FWI (Sajeva et al. 2014a; Gao et al.,

2014; Tognarelli et al. 2015; Datta, 2015). In these applications a method to reduce the number of unknown parameters and a highly efficient parallel implementation are crucial to make the computational cost of the stochastic inversion affordable (Diouane et al. 2014; Sajeva et al. 2014a). The extension of this two-step approach, based on a global (low-resolution) inversion followed by a local (high-resolution) inversion, to the elastic case is not the topic of the present work but deserves deeper investigation.

Many global derivative-free methods perform a wide exploration of the multidimensional parameter space and collect many different models. However, it is the single model producing the best fit with the observed data that focuses our attention, while the other models are often neglected. In this way, we fail to quantify the uncertainty that characterizes the final result. Instead, inverse problems can be solved in a probabilistic framework (Dujindam, 1988; Tarantola, 2005) in which the final solution is represented by posterior probability distributions (PPDs) in model space (see Appendix A for a brief review of the Bayesian formulation of inverse problems).

Among the many global search methods that have been proposed to solve 1D full-waveform inversion, we choose to apply genetic algorithms (GA's). Likewise other global search algorithms, GA's are not a Markov Chain Monte Carlo (MCMC) method (Rubinstein and Kroese, 2011), and a biased PPD is estimated if directly computed from the set of GA-sampled models and their associated likelihoods. To derive an unbiased PPD estimation, a simple grid-search method or a more sophisticated MCMC algorithm must be applied (Sen and Stoffa, 1996). However, the direct application of these methods is not feasible for high dimensional model spaces due to their high computational costs. Therefore, several methods that follow the solution of 1D FWI by means of GA optimizations (Sen and Stoffa, 1996; Mallick, 1999; Hong and Sen, 2009) or via local optimizations (Gouveia, and Scales, 1997, 1998) have been developed to obtain reliable and unbiased estimates of the posterior distributions. Another strategy based on ensemble Kalman filter (Evensen, 2009) has been proposed in the context of 1D elastic FWI to reduce the number of unknowns and to perform a statistical analysis of the final result (Jin et al. 2008).

In the present study, we combine an implementation of the GA method with a resampling of the explored model space by means of a MCMC method known as Gibbs Sampler (GS) (Geman and Geman, 1984). This hybrid approach attempts to combine the speed of GA's and the unbiased nature of GS to obtain reliable estimates of the uncertainties that affect the final result. In particular, the GS exploits all the models and their respective likelihoods that were collected during the GA inversion to compute the posterior probability distributions in model space. Sambridge (1999) proposed the same hybrid strategy in the context of neighbourhood algorithm inversion. However, as discussed in Sajeva et al. (2014b), the neighbourhood algorithm seems to show a slower convergence compared to GA in solving 1D elastic FWI.

To achieve a reliable estimation of the posterior probability distributions, the first step of GA optimization must perform a wide exploration of the model space because an insufficient GA sampling of the model space cannot be compensated for by the subsequent GS step. In this regard, GA optimization suffers from the "genetic drift" effect (Goldberg and Segrest, 1987; Horn, 1993), which limits the exploration of the model space and may guide the algorithm to prematurely converge toward a local minimum. To address this issue, we apply a GA implementation that combines the Niched-GA (N-GA) method with other mechanisms, such as migration, competition between subpopulations, and the stretching of the fitness function to maximize the exploration of the model space and to reduce the genetic drift.

In this work, the GA+GS approach for FWI is applied to derive a complete elastic characterization of the subsurface, assuming wave propagation in 1D elastic models. We start with a brief summary of genetic algorithms that introduces the reader to our particular implementation of GA optimization. Then, we discuss an example on an analytical misfit function to demonstrate the applicability of the hybrid method and the importance of attaining a wide exploration of the model space during GA optimization. The next section illustrates a synthetic FWI example in which the number of layers and their thicknesses are assumed to be known to avoid the overparameterization of the inverse problem (Sen and Stoffa, 1991). This simple synthetic example allows us to

demonstrate the capability of our peculiar GA implementation to attenuate the genetic drift and to maximize the exploration of the model space. To this end, we make use of self-organizing maps (de Matos et al. 2006) to visualize and compare the different model space explorations that are produced by standard GA and by our GA implementation. The second synthetic example is more complex because the 1D elastic model is derived from actual well log data. As in Mallick and Dutta (2002), we overcome the over-parameterization problem by fixing the layers' thicknesses to constant values based on the dominant frequency that characterizes the observed seismic data. Finally, we present a field case inversion that is performed on a single shot gather that was extracted from a Well Site Survey (WSS), where no a priori information in the form of borehole logs or geotechnical data is available. In all the FWI examples that we discuss, the reflectivity algorithm (Kennett, 1983) is used for forward modelling.

A brief introduction to genetic algorithms

Genetic algorithms are search algorithms based on the mechanics of natural selection and evolution according to the Darwinian principle of "survival of the fittest" (Holland, 1975). The GA optimization process is always driven by three main genetic operators: selection, cross-over and mutation. A population of individuals, which encodes candidate solutions to an optimization problem, evolves toward better solutions by starting from a population of randomly generated individuals. The fitness, namely, the goodness of each candidate solution, is evaluated in each iteration (or "generation"), and then multiple individuals are stochastically selected from the current population based on their fitness (models with higher fitness are more likely to be selected). The selected models are then modified (using crossover and mutation operators) to form a new population, which is used in the next iteration.

In the fitness assignment, each individual in the selection pool receives a reproduction probability depending on its own misfit value and the misfit values of all the other individuals. The fitness value for each individual can be determined either directly from its associated misfit or by

applying a rank-based fitness assignment. Bäck and Hoffmeister (1991) observed that the latter approach is more robust than proportional fitness assignment and thus is the method that is applied in this work. In the successive step, the models are selected for reproduction and several selection methods can be used to this goal. See Goldberg and Deb (1991) or Blickle and Thiele (1995) for an extensive comparison and discussion about selection schemes that can be used in a GA optimization. The next step of cross-over produces new individuals by combining the information (namely, the value of each variable) of two or more parents. Finally, in the mutation step randomly created values are added to the variables with a low probability to prevent premature convergence and to escape from local minima. After the parents have been subjected to these operations, the generated offspring has to be reinserted to replace the parents to form the new population. We use an elitist reinsertion, which preserves the fittest individuals of the previous generation in the new generation, combined with a fitness-based reinsertion in which the lowest-fitness parents are replaced by higher-fitness offspring.

Our GA implementation and the hybrid GA+GS method

In this work, we adopt a more sophisticated version of GA that is called a niched GA (N-GA), which is based on the punctuated equilibria evolutionary theory (Gould and Eldredge, 1977). According to this method, the initial random population is divided into multiple subpopulations, which are subjected to separated selection and evolution processes (Goldberg, 1989; Mitchell, 1998). The N-GA method has been demonstrated to avoid the genetic drift effect (Horn, 1993), which is the loss of diversity inside a single population that can lead to a local minimum in the case of multimodal misfit functions.

To further improve the exploration of the model space, we apply different evolution strategies for different subpopulations. Therefore, the entire set of subpopulations evolves according to different selection methods, mutation operators and fitness assignment methods. Tanese (1987) demonstrated that this approach, in which different evolution strategies are simultaneously applied,

165 increases the capability of GA to explore the entire model space. In addition to these strategies, we shrink the mutation range and stretch the fitness function (Sen and Stoffa, 1991, 1992) by increasing the selective pressure in each generation. The mutation range is the range that contains
168 the admissible values that a mutated variable can assume, whereas the selective pressure is the probability of the best individual to be selected compared with the average selection probability of all individuals. In particular, we set a small selective pressure value for the initial generations to
171 ensure maximum genetic variance within each subpopulation. In this way, models with similar fitness values have similar likelihoods of being selected, which results in a more efficient and wide exploration of the model space. Conversely, we set a higher selective pressure at the end of the
174 inversion, when the most promising zones of the misfit function have been reached. In this way, minor differences in the fitness values are exaggerated, which results in a fine tuning of the solution. In the following FWI tests, the selective pressure linearly increases with the number of
177 iterations. We also adopt competition between subpopulations, where the best fitting subpopulations are awarded with some individuals from the less-fitting ones to better explore the most promising portions of the model space (Schlierkamp-Voosen and Mühlenbein, 1996).

180 The FWI tests that follow are quite similar in terms of the number of unknowns (21 and 60 unknowns in the two synthetic inversions and 48 in the field data inversion) and thus we can keep the same GA setting for all the tests. In particular, we use a population of 400 individuals, which
183 evolves into 40 generations and is divided into 10 subpopulations, for more than 13000 forward model evaluations. In all cases, we apply a selection rate of 0.8 (we select 80% of the parents for reproduction) and a mutation rate that is the reciprocal of to the number of unknowns, whereas
186 migration and competition between subpopulations occur every 8 and 5 iterations, respectively. Concerning the mutation rate Schlierkamp-Voosen and Mühlenbein (1993), performing GA optimizations and considering from 2 to 100 unknowns, demonstrated that the best choice for the
189 mutation rate is the reciprocal of the number of unknowns. In this way, on average, just one variable for each individual is mutated per iteration. In the following examples, the classical L_2 norm

between observed and modelled seismic data is considered as the misfit function. In all cases, different evolution strategies for each subpopulation, stretching the fitness function and shrinking the mutation range, are included during the iterations. In particular, among the many rank-proportionate selection methods available, we use the stochastic universal sampling, roulette wheel selection and tournament selection methods and we apply linear and non-linear fitness assignments. More detailed information about these and other GA principles can be found in Goldberg (1989), Mitchell (1998) or Sivanandam and Deepa (2008).

There is no unique rule to set the GA parameters, as the best GA setting strongly depends on the problem under examination and in particular on the number of unknowns and on the complexity of the misfit function. For these reasons the best setting for the GA parameters is usually found by trial and error. Basing on our experience on GA optimization for FWI, the heuristic rules we have followed are briefly summarized below. The number of individuals must be always higher than the number of unknowns: in case the misfit surfaces are complicated, it should be 10 or 20 times the number of unknowns. Instead, in case of simple convex misfit surfaces 2 or 3 times the number of unknowns should suffice. Also the choice for the number of subpopulations strongly depends on the number of local minima that we suppose characterizes the misfit function. In our experiments, we found that 5 to 10 subpopulations are required for performing an efficient exploration of the model space. Concerning the selection rate, we found that a value between 0.8-0.9 is usually a good compromise between preserving genetic variance and ensuring an efficient selection process. Different criteria can be used to stop a GA optimization. For example the inversion can be stopped when no further improvements can be seen in the data misfit evolution. This is the stopping criterion adopted in this work. Another possible stopping criterion is based on the difference between the mean and the minimum data misfit. In fact, as noted by Reeves and Rowe (2002), the approaching of mean misfit toward the minimum misfit indicates a loss of genetic diversity. When the genetic diversity is low, the genetic optimization is less efficient and it may be convenient to stop the inversion.

Once the GA inversion has stopped, it is possible to create an approximate PPD for the GA solution (Sen and Stoffa, 1992) that we name the GA PPD, which, as previously said, suffers from several limitations. Therefore, we apply the Gibbs sampler method to efficiently estimate the PPD for each variable. The mathematical formulation of the GS step is detailed in Sambridge (1999) together with recipes for practical applications. Thus, only a brief summary is given in Appendix B. To derive the final PPD, the explored model space is divided into Voronoi cells that are centred on each model found by the GA inversion and the likelihood value of the model is assigned to the whole cell. The model space is then resampled by running a Gibbs sampler, which extracts a sequence of random samples from a specific probability distribution. The GS algorithm is frequently applied when direct sampling is difficult, such as when the analytical formulation of the distribution is not known explicitly and it is only numerically defined. The sequence of random samples is used to approximate the joint or the marginal distributions of the variables. Other authors have demonstrated (see, for example, Gelman et al. 2013) that the sequence of samples drawn by a GS algorithm constitutes a Markov chain. Because the likelihood values that are required by the Gibbs sampler are known from the approximate GA PPD, no additional forward model is needed. This characteristic is particularly important because it determines the low computational cost of the GS step.

In general, multiple GS walks are sequentially performed to increase the reliability of the results, and the results of each step are combined to derive the final probability distributions. However, the samples drawn at the beginning of the chain (during the so called “burn-in period”) may not accurately represent the desired distribution (Sambridge, 1999). Therefore, we do not include these samples in the evaluation of the final PPD. In the following inversion examples, we use 100 different GS walks in which 2000 random samples are drawn from the GA PPD. From these 2000 samples, only the second half is used to compute the final probability distributions. During the computation of final PPDs, we consider uninformative prior distributions that are uniformly distributed over the entire search range for each inverted parameter. In this context, the final

probability distributions are mainly determined by the likelihood functions (see Appendix A for further details). To verify if the Gibbs sampler has reached a stable distribution, it is important to check the Potential Scale Reduction (PSR) factor (see Appendix B) which gives an indication on the reliability of estimated PPDs.

Testing the GA+GS method on an analytical function

We perform a test that uses an analytical function to demonstrate the potential of this hybrid approach to attain an unbiased estimation of the marginal and joint posterior probability distributions. In this test, the GA+GS method is employed to draw samples from a 2D joint PPD $p(x_1, x_2)$ with a double peak structure, taken from Hong and Sen (2009). Due to the simplicity of the function, and to evidence the need of an accurate exploration of the model space, we employ a standard single-population GA optimization instead of the more sophisticated implementation that was previously described. This simple 2D example allows us to compare both the true joint PPD and the joint PPD that is estimated by the GA+GS method. As shown in equation 1, the considered PPD is the sum of two bivariate normal distribution probability density functions $PDF_1(x_1, x_2)$ and $PDF_2(x_1, x_2)$, in which a factor of 0.5 ensures that the resulting posterior distribution is properly normalized:

$$PDF(x_1, x_2) = 0.5\left[PDF_1(x_1, x_2) + PDF_2(x_1, x_2)\right] \qquad (1)$$

The bivariate normal distribution of equation 1 can be re-written in the following form:

$$PDF(x_1, x_2) = \frac{1}{2\pi\sqrt{(1-\rho^2)\sigma_{11}\sigma_{22}}} \exp\left[\frac{-z}{2(1-\rho^2)}\right] \qquad (2)$$

where σ represents the covariance matrix:

$$\sigma = \begin{bmatrix} \sigma_{11} & \sigma_{12} \\ \sigma_{21} & \sigma_{22} \end{bmatrix} \qquad (3)$$

ρ is the correlation coefficient of x_1 and x_2 as defined in the following equation:

$$\rho = corr(x_1, x_2) = \frac{\sigma_{12}}{\sqrt{\sigma_{11}\sigma_{22}}} \qquad (4)$$

and z is equal to

$$z = \frac{(x_1 - \mu_1)^2}{\sigma_{11}} - \frac{2\rho(x_1 - \mu_1)(x_2 - \mu_2)}{(\sigma_{11}\sigma_{22})^{0.5}} + \frac{(x_2 - \mu_2)^2}{\sigma_{22}} \qquad (5)$$

The analytical distribution $PDF_1(x_1, x_2)$ is characterized by a mean vector equal to $\mu = (0,0)$ and a covariance matrix equal to

$$\sigma = \begin{bmatrix} 1 & 0 \\ 0 & 1 \end{bmatrix} \qquad (6)$$

The matrix in equation 6 indicates that x_1 and x_2 are uncorrelated to each other and thus the correlation coefficient is 0. The distribution $PDF_2(x_1, x_2)$ has a mean vector of $\mu = (4, 0)$ and a covariance matrix given by

$$\sigma = \begin{bmatrix} 2 & 0.8 \\ 0.8 & 2 \end{bmatrix} \qquad (7)$$

Therefore, x_1 and x_2 are correlated to each other in this case, with a correlation coefficient equal to 0.4. By summing $PDF_1(x_1, x_2)$ and $PDF_2(x_1, x_2)$ as described in equation 1, the resulting joint $PDF(x_1, x_2)$ is a bimodal surface (Figure 1a) with one peak at (0,0) and the second peak at (4,0).

In Figure 1, we give a visual representation of the different steps that characterize the GA+GS approach. Figures 1a and 1b represent the analytical *PDF* and the ensemble of 1000 models (white dots) that result from the GA optimization on the joint *PDF* $p(x_1, x_2)$, respectively. The Voronoi cells, which divide the entire model space that is explored by the GA optimization, are shown in Figure 1c, while the multiple GS walks that are used to draw random samples from the GA PPD are illustrated in Figure 1d. According to Sambridge (1999), the random GS walks allow the computation of the final GA+GS estimation of the PPD. As expected, the sampling performed by the GS algorithm is denser in the upper left corner of Figure 1d, which is where the GA's focused the exploration of the model space. However, the GS, differently from the GA sampling, respects

288 the importance sampling principle (Rubinstein and Kroese, 2011) and allows for a highly accurate estimation of the final posterior probabilities.

The marginal PPD is a projection of the joint PPD to a particular parameter axis and can be 291 obtained by integrating out all the other parameters. The true marginal PPDs for x_1 and x_2 are shown by the green lines in Figures 2a and 2b, respectively. The marginal PPD for x_1 is a bimodal distribution, whereas that for x_2 is a univariate normal distribution. We now aim to compare the 294 marginal and joint PPDs that are estimated after the GA optimization and GA+GS method with the true values. To this end, we compute the marginal GA PPDs on the GA ensemble of 1000 models (orange bars in Figures 2a and 2b) following Sen and Stoffa (1992). We then refine the marginal 297 GA PPDs by running a GS to derive the final GA+GS marginal PPDs (blue curves in Figures 2a and 2b).

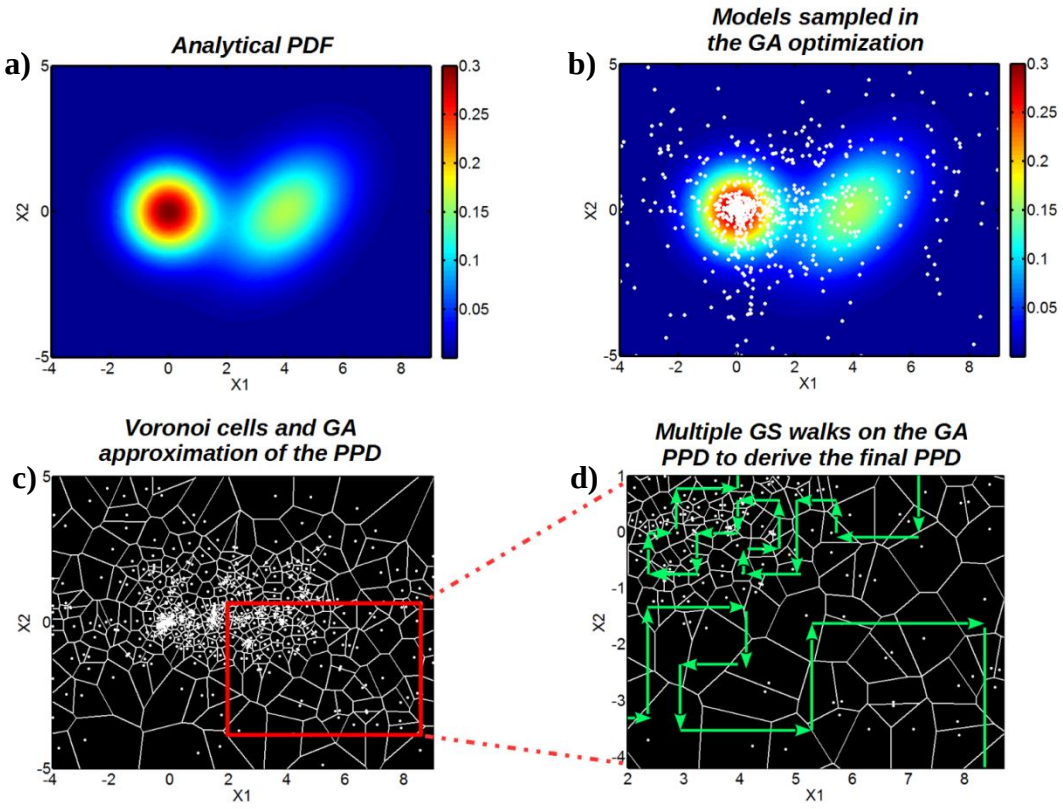

300 *Figure 1: Examples of the different steps that characterize the hybrid GA+GS approach. a) The initial analytical PDF used in the optimization. b) The 1000 models (white dots) sampled during the GA optimization. c) The model space portion explored during the GA step is divided into Voronoi*

303 *cells (delimited by the white lines), and the likelihood that is associated with each explored model is assigned to the entire cell. This step results in the GA approximation of the PPD. d) Multiple GS walks (examples of GS walks are illustrated by the green paths) are used to draw samples from the*
306 *GA approximation of the PPD. This step gives the final PPD that was estimated by the GA+GS approach.*

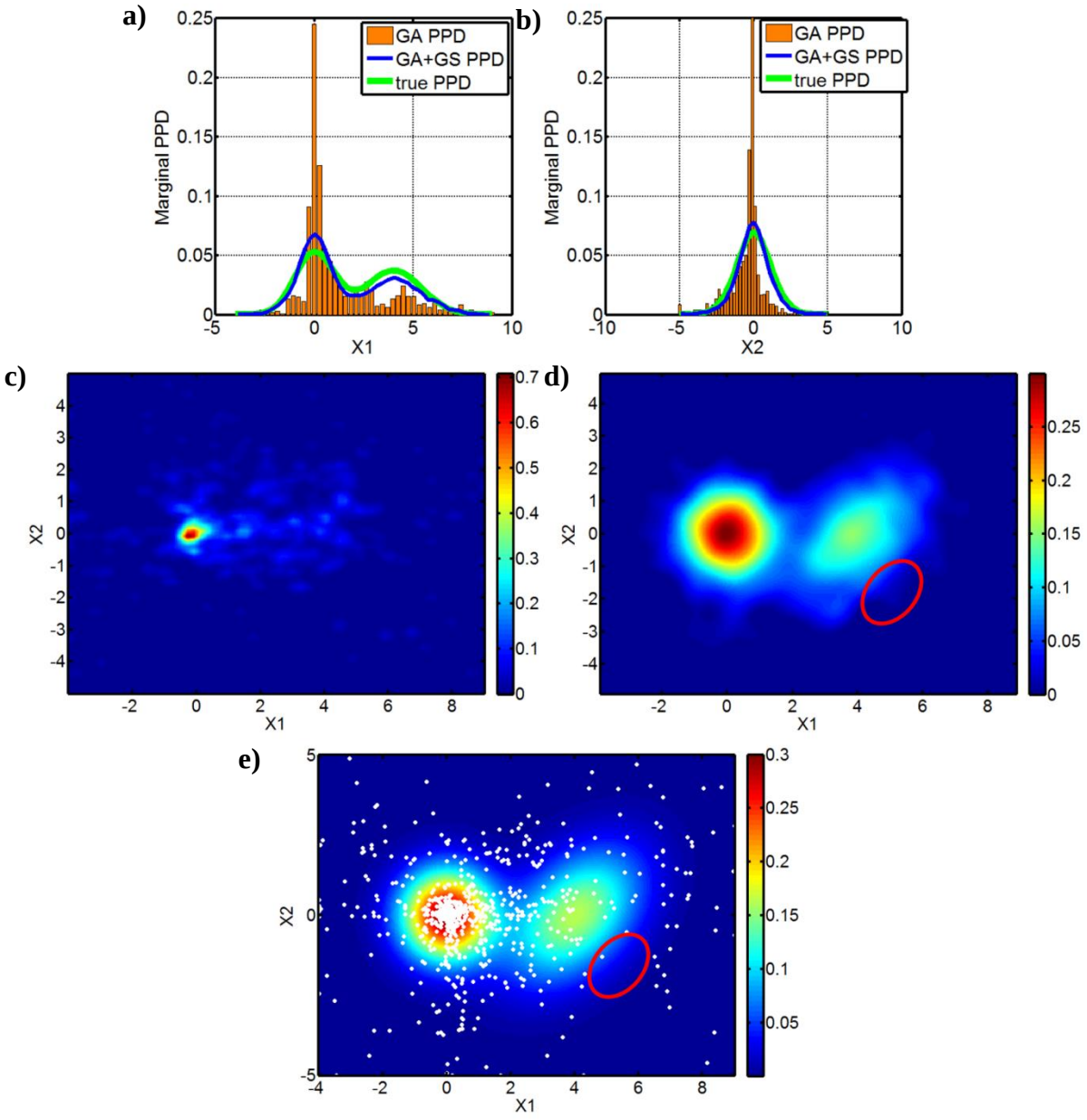

309

Figure 2: In a) and b), comparisons are shown for the variables x_1 and x_2 from the true marginal distributions (green lines), the marginal PPDs that were estimated by the GA method (orange bars)

312 *and the GA+GS marginal PPD estimations (blue lines). c) The GA approximation of the joint distribution. Note the strong underestimation of the uncertainties that resulted from the oversampling of the model space region with the highest probability. d) The final joint PPD* 315 *estimated by the GA+GS method (compare with the true joint probability distribution shown in e) and the GA joint estimation shown in 1c). Note the different colour-scale in c) and d). e) The true joint posterior distribution (in colour) defined by equation 1 and represented in Figure 1a. The* 318 *white dots represent the 1000 models sampled in the GA optimization. The red circle in d) and e) marks the area where the differences between the true and estimated GA+GS joint PPDs are more prominent. See the text for additional comments.*

321

The GA method tends to oversample the region with high probability and thus underestimates the true uncertainties. In contrast, the hybrid GA+GS method yields marginal PPD estimations that 324 are very similar to the true values. The joint GA PPD (Figure 2c) severely underestimates the variance that is associated with the inverted parameters, whereas it strongly overestimates the probability that is associated with the peak at (0,0). Moreover, the bimodality of the true distribution 327 and the correlation between x_1 and x_2 in the $PDF_2(x_1, x_2)$ in this approximated PPD are completely lost. Instead, the GA+GS joint PPD that is shown in Figure 2d nicely matches the true joint probability distribution of Figure 2e. Figure 2d also shows that the GA+GS method can predict the 330 correlation between x_1 and x_2 in $PDF_2(x_1, x_2)$ as evidenced by the slope of the estimated PPD near the secondary peak at (4,0). The main differences between the true and the GA+GS joint PPDs occur in the areas that are highlighted by the red circles in Figures 2d and 2e. In fact, the PPD 333 values in Figure 2e are between 0.05 and 0.1, whereas those in Figure 2d are very close to zero, which indicate an underestimation of the PPD function due to an insufficient sampling by the GA method (the GA's sampled only two models in this area). Therefore, the importance of an accurate 336 exploration of the model space in the GA optimization, which the standard GA method was unable to perform, is confirmed. This justifies our efforts in implementing an efficient GA that avoid the

genetic drift effect. However, this analytical example also demonstrates that the hybrid GA+GS algorithm is a reliable method for uncertainty analysis.

First synthetic example: exact parameterization

The reference model is a geological sequence that was extracted from the Ocean Drilling Program (ODP) database (http://www-odp.tamu.edu/) and includes a total of eight layers, whose thicknesses, P-wave velocities (*Vp*), S-wave velocities (*Vs*) and densities are shown in Figure 3 (black curves).

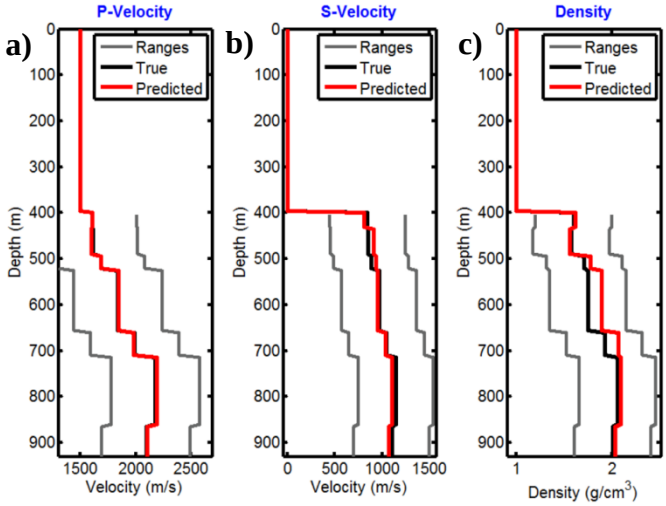

Figure 3: Comparison between the true (black) and predicted (red) elastic properties (a, b and c for Vp, Vs and density, respectively). The grey lines show the parameter ranges used during the inversion.

The reference synthetic seismogram, which was computed by the reflectivity method, consists of 30 traces that are spaced by 100 m with a minimum offset of 100 m. The source signature is a 5-Hz Ricker wavelet. To estimate the capability of our algorithm to explore the model space, we set a wide search range for each parameter: +/- 400 m/s for *Vp* and *Vs* and +/- 0.4 g/cm^3 for density, centered around the true parameter values.

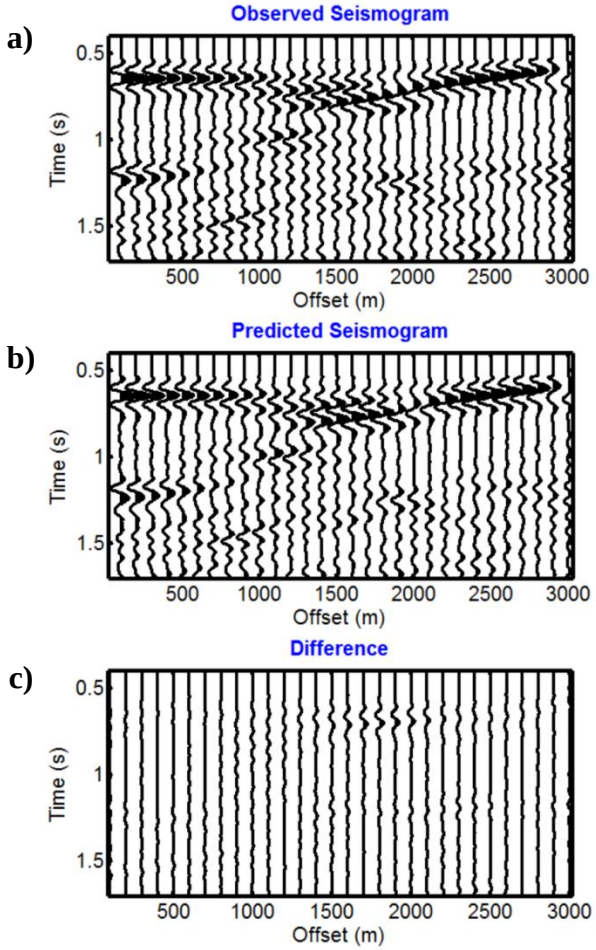

357 *Figure 4: a) Observed seismogram, b) best predicted seismogram and c) their difference. The seismograms are NMO-corrected for the water velocity and are represented with the same amplitude scale.*

360

Overparameterization is a well-known issue in inverse problems, which is caused by too many correlated unknowns being introduced into the inversion. For example, overparameterization can be 363 produced if the thicknesses and the number of layers are left unknown or by simultaneously inverting the P-wave velocity and the thickness of each layer. In fact, many combinations of *Vp* and layer thickness give rise to almost identical reflection kinematics. The overparameterization 366 severely aggravates the ill-posedness of the inverse problem and increases the number of local minima in the misfit function. To avoid overparameterization in this example, we set the layer thicknesses and the water properties to their true values.

Figures 3a, b and c show a comparison between the best predicted model and the true one. The *Vp* values are totally recovered, whereas the results are less accurate for *Vs* and, particularly, for density. Figures 4a, b and c show the observed and best predicted seismograms and their difference, respectively. Note the good results in terms of data misfit. Figures 5a, b and c show the evolution of the mean model misfit (blue curve) and the minimum model misfit (red curve) that were computed when considering the entire set of ten subpopulations for the *Vp*, *Vs* and density, respectively. The model misfit is computed as follows:

$$Model\ Misfit = \frac{1}{N}\sum_{i=1}^{N} | m_i^{true} - m_i^{pre} | \qquad (8)$$

where N is the total number of layers (excluding the water column) and m^{true} and m^{pre} are the true and current predicted models, respectively. The final model misfit for *Vp* (Figure 5a) is smaller than the *Vs* model misfit, and the evolution of the *Vs* and density model misfits are characterized by more irregular trends that indicate that the seismogram is more sensitive to *Vp* perturbations than to variations in the other two variables. The differences between the mean and minimum model misfit curves tend to decrease during the inversion as the algorithm converges to a good fitting model.

The 10 subpopulations show different data misfit evolutions (Figure 5d) as they explore different parts of the model space. Jumps occur when competition and migration take place. The evolution of the number of individuals for each subpopulation is shown in Figure 5e: all of the subpopulations have the same number of individuals (40 individuals) in the first iteration, and this number changes every 5 iterations when competition occurs. Due to competition, the most successful subpopulations (those that explore the most promising portion of the model space) attract individuals from the less successful ones. At the end of the inversion, the best subpopulation (number 8, yellow curve in Figure 5e) has more than doubled its number of individuals. Conversely, fewer than 20 individuals remain in the worst subpopulation (number 10, red curve in Figure 5e).

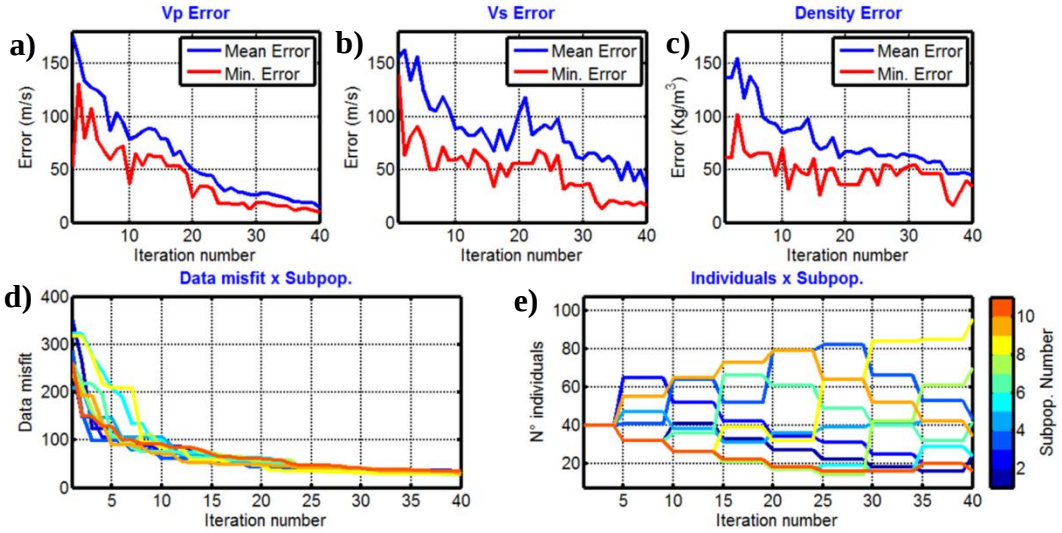

393 *Figure 5: Evolution of the mean and the best model misfit for the Vp, Vs and density parameters as a function of iteration number (a, b and c, respectively). Evolution of the data misfit (d) and the number of individuals (e) for each subpopulation.*

396

Figure 6 shows a comparison between the GA approximation of the marginal PPD (orange bars) and the marginal probability distribution for each model parameter that is estimated by combining 399 the GA and GS methods (cyan filled curves). The posterior marginal distributions of the density are often multimodal and flat, which indicates that multiple values of this parameter generate seismograms with almost identical data misfit. Conversely, the peak of the a posteriori distribution 402 that is estimated by the GA+GS method for *Vp* and secondarily for *Vs* is always very close to the true value. This figure makes clear that, as expected, the uncertainty that is associated with the elastic parameter estimation increases when passing from *Vp* to *Vs* and to density. The proposed GA 405 implementation returns marginal PPDs that, although they possess an underestimated variance with respect to the GA+GS method, are not characterized by a spiky appearance (as shown, for example, in Sambridge, 1999), meaning that the implemented GA method is able to efficiently explore the 408 model space.

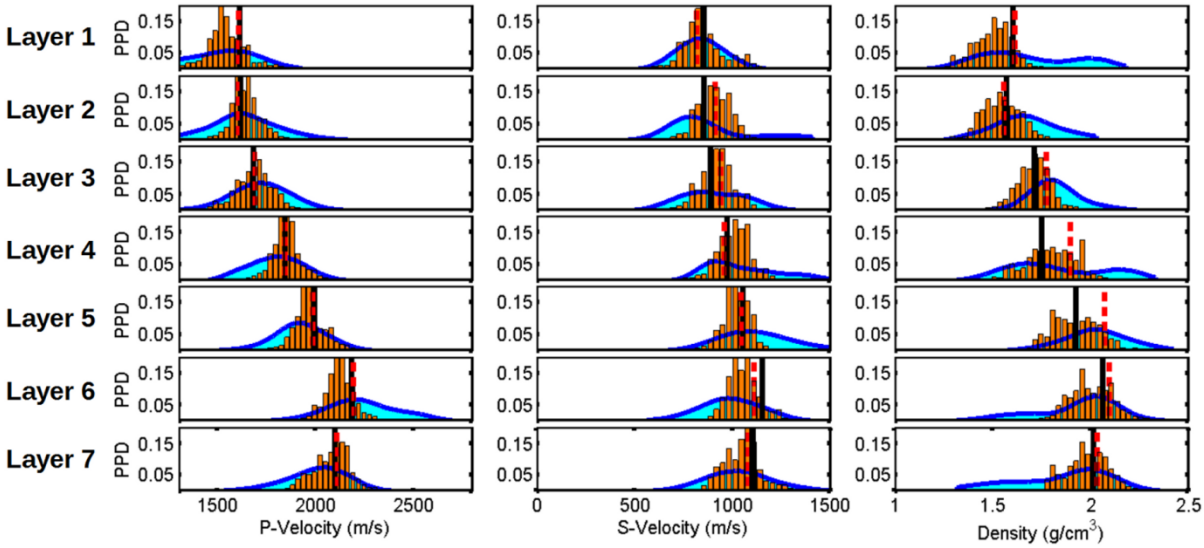

Figure 6: The GA approximation of the marginal PPDs (orange bars) and the final GA+GS estimation of the marginal distributions (cyan filled blue curves) are displayed from top to bottom for each inverted layer. The Vp, Vs and density values are represented in the left, central and right columns, respectively. The continuous black and dashed red lines illustrate the true and the predicted model parameters by the GA inversion, respectively. To better display the variance of each parameter, the x axes are represented with the same scale.

Figure 7 illustrates the posterior 2D marginal probability distributions estimated by the GA+GS for the fourth layer. Figures 7a and 7b display the 2D distributions projected onto the *Vp*-density and *Vs*-density planes, respectively. The bimodality that characterizes the density PPD and the inverse correlation between the *Vp* and density parameters are both evident in Figure 7a.

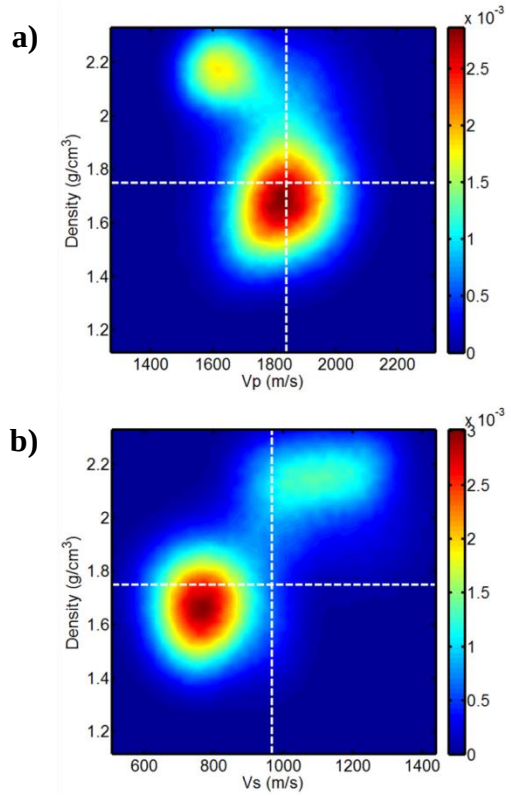

Figure 7: The posterior 2D marginal distributions for the fourth layer. The Vp-density and Vs-density distributions are shown in a) and b), respectively. The dotted white lines represent the true values. To better compare the resolution that is associated with each parameter, the axes are represented with the same scale.

The highest peak corresponds to a *Vp* of 1800 m/s and to a density of 1.7 g/cm³, which are very close to the true values (white dotted lines in the figure), whereas the secondary peak is located at lower *Vp* but at a higher density value, showing a negative *Vp*-density correlation. The higher resolution that characterizes the *Vp* estimation with respect to the density estimation is also evident. The positive correlation between *Vs* and density clearly stands out when examining the *Vs*-density 2D marginal distribution (Figure 7b): in this case, higher density values are associated with higher *Vs* values. The opposite parameter correlations that are shown in Figures 7a and 7b occur because we are trying to match not only the kinematics of the reflections but also their amplitudes. Concerning the amplitude of the reflections and considering the Aki and Richards equation (Aki

and Richards, 1980) for the P-wave reflection coefficient from a single interface (or other analogous equations), the *Vs* and density contrasts exert an opposite influence on the variation in the reflection
438 coefficient with incidence angle, while the *Vp* and density contrasts produce the same effects. Thus, to keep the variation in the reflection coefficient constant with incidence angle, an increase in the *Vs* contrast must be associated with an increase in the density contrast; conversely, an increase in the
441 *Vp* contrast must be associated with a decrease in the density contrast. Therefore, the GA+GS method was also able to recover the correct correlations among the inverted parameters.

444 **The proposed GA versus the standard GA implementation**

To better illustrate the benefits in terms of the wider exploration of the model space that characterize the proposed GA implementation, we repeat the FWI test that was described in the
447 previous section by using a standard, single-population GA. The main GA parameters (as the individuals for each generation, or the maximum number of generations) are the same as those in the previous example. Due to the high-dimensional model space, we use the clustering technique
450 that is known as self-organizing map (SOM; de Matos et al. 2006) to visualize the model space explorations that are performed by the two different GA implementations. In particular, the entire set of GA models up to a given iteration will constitute the input ensemble for the SOM algorithm.

453 The SOM method uses a net that is formed by neurons to compute the unified distance matrix (Ultsch, 1993), which is a 2D representation of a high-dimensional model space and helps to display clusters in high-dimensional spaces. In the following examples, we employ a particular
456 version of the unified distance matrix, the so-called “sample hits” plot, which indicates how many data points extracted from the input ensemble of explored models are associated with each neuron. Therefore, neurons associated with many data points can be thought of as a single cluster.

459 We aim to cluster the entire set of models generated up to a particular generation for the standard GA and the proposed GA implementation. Models that explore the same portion of the model space will be classified by the SOM algorithm as belonging to the same cluster. To analyse the different

462 evolutions of the model space exploration, the SOM clustering is performed with the models that were produced up to different generations serving as the input. The two examples start from the same initial random population and evolve for 40 generations. In Figure 8, the different explorations
465 of the model space in the two cases are represented by the sample hits plot. In this case, we used an 8x8 map that consists of 64 neurons distributed according to a hexagonal topology. In Figure 8 the dimension of each violet hexagon is proportional to the number of input models that are associated
468 with each neuron.

As expected, the distribution of the randomly generated models is fairly even in the initial generation (Figure 8a). However, comparing the evolutions of the two GA implementations after
471 fifteen generations shows that the standard GA method has already restricted its exploration to limited portions of the entire model space (Figure 8b), while the GA implementation we use is still exploring different sectors of the model space (Figure 8c). This characteristic of the standard GA
474 method is confirmed at the last generation (Figure 8d), when most of the models generated during the inversion are localized to a single restricted portion of the entire model space, evidencing the genetic drift effect. Conversely, the proposed GA implementation has performed a wider model
477 space exploration as indicated by the many different clusters at the end of the 40 generations (Figure 8e).

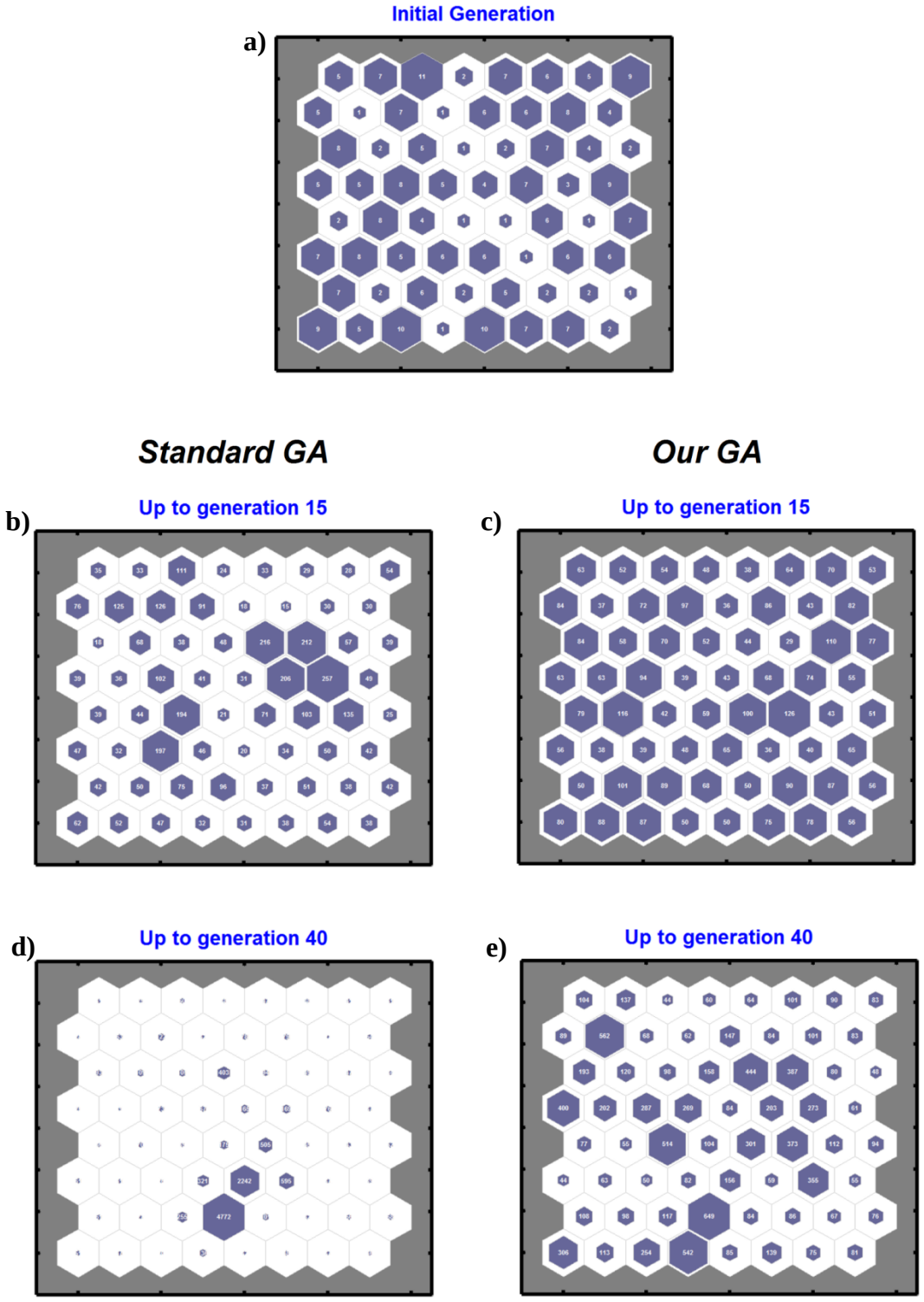

Figure 8: Sample hits plots that represent the different evolutions of the standard single-population and our GA implementation. Each plot is generated by clustering the entire set of generated models up to a certain generation and projecting the result to a two-dimensional map (see the text for more details). The two tests start from the initial, randomly generated population of models (a). The evolution of the standard single-population GA case is represented in b) and d),

whereas c) and e) represent the evolution of our GA inversion. This figure demonstrates that the proposed GA implementation is characterized by a wider exploration of the model space compared with the standard GA method.

Second synthetic example: underparameterization

Any attempt to exactly parameterize the subsurface will, in fact, be an underparameterization because the layers in real media are thinner and far more numerous than modelled layers (Sen and Stoffa, 1991). Starting from this basic knowledge, we consider a depth model that is derived from actual well log data of *Vp*, *Vs* and density. In particular, by making use of the Backus averaging method (Backus, 1962) and considering a source wavelet with a dominant frequency of 50 Hz and the minimum velocity of the log, we scale the log data to the seismic scale by determining an equivalent depth model with constant layer thicknesses of 3 m (Figure 9, black curves). On this scaled model, we computed a synthetic seismogram that constitutes our observed data.

In the following inversion, the forward modelling is performed by considering the same source signature but with a dominant frequency of 15 Hz. Knowing that the expected maximum resolution of 1D FWI is between 1/4 and 1/6 of the maximum wavelength associated with the dominant frequency (Mallick and Dutta, 2002), we fix the layer thicknesses of the inverted model to 20 m, that is, to 1/5 of the maximum wavelength. In the data misfit calculation, the modelled data are compared with a low-pass filtered version of the observed seismogram. In this example, the range of admissible values for *Vp*, *Vs* and density are set within ranges of 800 m/s and 0.8 g/cm^3 for the velocities and density, respectively (Figures 9a, b and c, grey lines), which are centred on heavily smoothed versions of the original logs. Both the GA setting and the seismic acquisition parameters are the same as those in the first example.

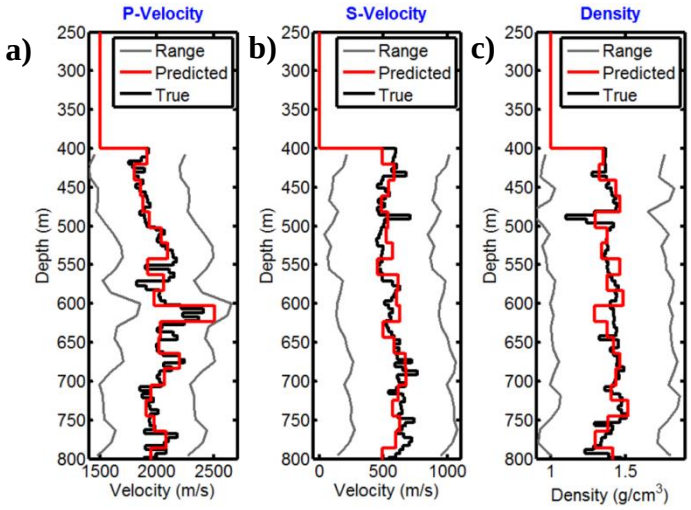

Figure 9: Comparison between the true (black) and the predicted (red) elastic properties (a, b and c). The black curves represent the log data after Backus averaging for a dominant frequency of 50 Hz. The red curves indicate the predicted elastic properties for a dominant frequency of 15 Hz. The grey lines show the inversion parameter ranges that have been defined around a highly smoothed version of the original log data.

The trends of the predicted properties (red lines in Figures 9a, b and c) reproduce the true elastic properties despite the different resolutions. As expected, the P-wave velocity shows a better match, while the results are less accurate for *Vs* and particularly for density. The inversion was able to reconstruct the numerous sudden increases and reversals that occur in the true *Vp* profile. Figures 10a, b and c demonstrate the good fit between the observed and predicted seismic data in the frequency bandwidth considered in the inversion.

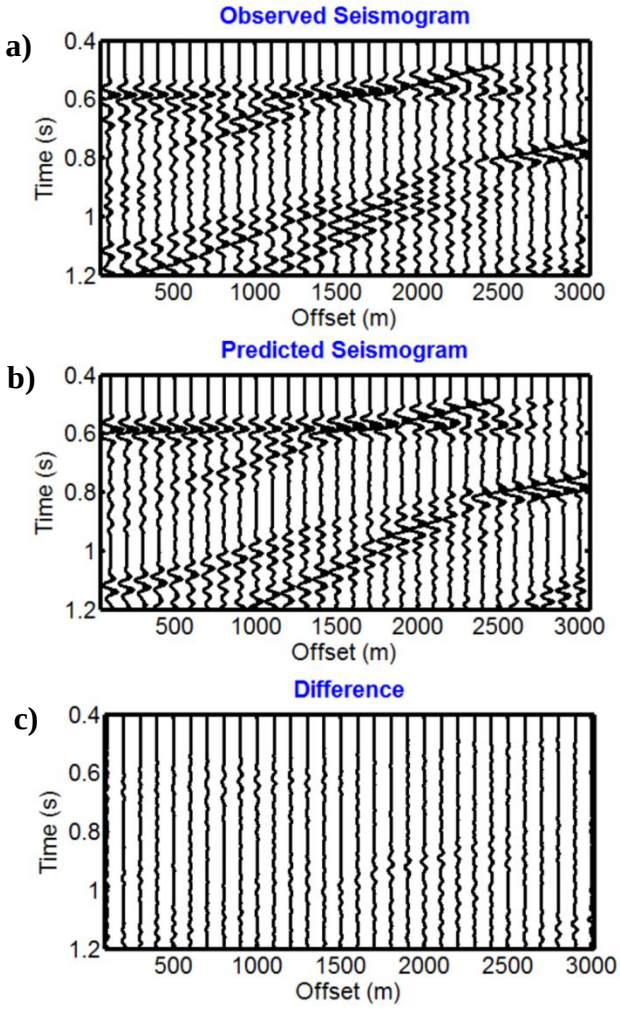

Figure 10: a) Observed seismogram, b) best predicted seismogram and c) their difference for the same frequency range during the inversion (which determines the layer thickness of the inverted model). The seismograms are NMO-corrected for the water velocity and are represented with the same amplitude scale.

Figure 11 illustrates a comparison between the GA and GA+GS estimation of the marginal probability distributions for the first seven layers (excluding the water column, whose properties are assumed to be known during the inversion). The conclusions that are drawn from the first example still remain valid in this more realistic test: the density remains the less-resolved elastic parameter and the GA method underestimates the uncertainty that is associated with each inverted parameter.

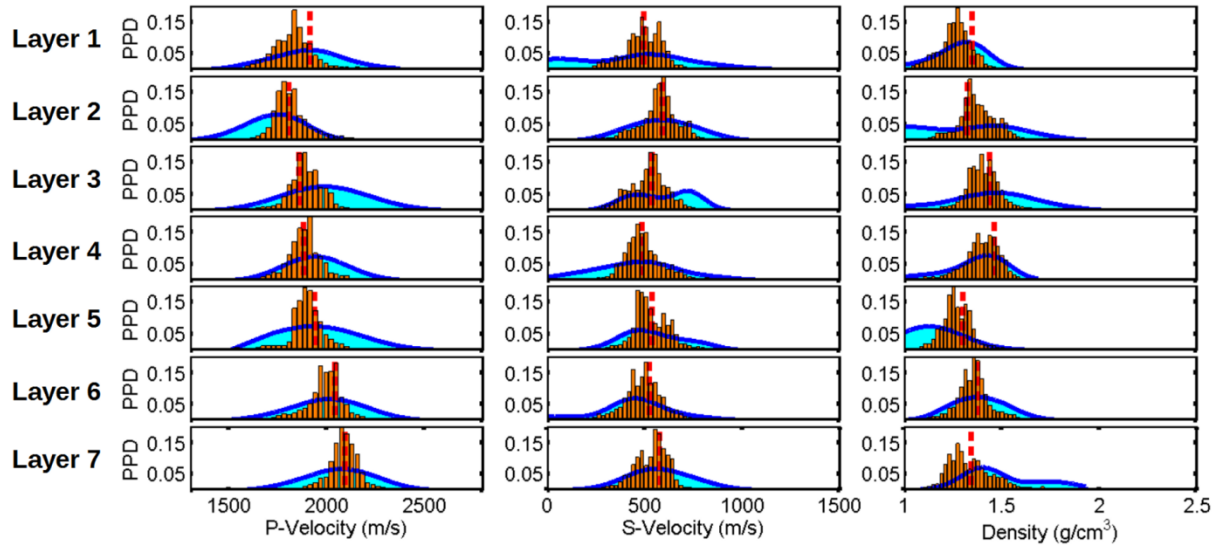

Figure 11: The GA approximation of the marginal PPDs (orange bars) and the final GA+GS estimation of the marginal distributions (cyan filled curves) are shown from top to bottom for the first seven layers. The Vp, Vs and density values are represented in the left, central and right columns, respectively. The dashed red lines show the predicted model parameters by the GA inversion. To better display the variance of each parameter, the x axes are represented with the same scale.

Third example: inversion of field data

Finally, we apply the hybrid GA+GS inversion to a field common shot from a marine well site survey, which is characterized by a 1 ms sampling interval, 20 m minimum offset, 12.5 m group interval, 607.5 m maximum source-receiver distance and 0.6 s recording length. The limited maximum offset and the simple layered nature of the shallow strata make the assumption of a 1D model realistic. As for the previous synthetic example, we low-pass filter (0 – 37 Hz) the shot gather used in the inversion, yielding a vertical resolution of 20 m, which we fix as the thickness of the layers in the inverted model. The source signature used in the inversion is taken from the recordings of an auxiliary channel that contains the source pulse for each shot. The GA setting is the same as that used in the previous tests, which results in a total number of individuals (that is, of the explored models) equal to 13200.

The velocities that are determined from standard velocity analysis define the *Vp* trend, whereas the *Vs* and density trends are empirically scaled values from *Vp*, which are defined from the lithological and geological context of the explored area (a shallow water shale-sand sequence). The admissible parameter ranges in the inversion are +/-300 m/s for *Vp* and *Vs* and +/-0.3 g/cm^3 for density and are centred around their respective trends.

The results are illustrated in Figures 12a, b and c. We observe a linear and gradual increase for all the parameters and a significant *Vp* jump at 280 m, which is associated with a density decrease. We cannot be totally confident in the density estimates due to the ambiguities in the density estimation and the cross-talk between velocity and density. Moreover, independent or additional data such as well log recordings or geotechnical data are not available to validate the results.

Figures 13a, b and c show the observed seismogram, the best predicted seismogram and their difference, respectively. Given the noise contamination, the absence of any pre-processing and the elastic 1D assumption, the match between the predicted and observed data is reasonable. The evolutions of both the data misfit and the number of individuals for each subpopulation are depicted in Figures 14a and 14b, respectively. Figure 14a shows that the trends of the different subpopulations nicely merge and assume a rather flat attitude after approximately 20/25 iterations, indicating that convergence has been attained. The evolution of the number of individuals for each subpopulation is illustrated in Figure 14b. Figure 15 shows a comparison between the GA and GA+GS estimation of the marginal distributions for the first seven layers (excluding the water column, whose properties are assumed to be known). In contrast to the synthetic examples, the final GA+GS marginal PPD estimations in this more challenging test appear more complex, and an increase in the uncertainties and ambiguities is visible for all parameters but is particularly evident for the density. The overall higher ambiguity in the parameter estimations may be ascribed to noise contamination in the observed data but can also be due to the physical assumptions that were made in the forward modelling computation (e.g., perfectly elastic propagation, homogeneous and isotropic 1D media), which may not be totally verified in this specific case. Moreover, the very low

resolution that is associated with the density estimations is also related to the limited offset range that characterizes this WSS acquisition. However, for the purposes of this paper, this test confirms
579 that the posterior marginal probabilities that are derived from the GA-sampled models strongly underestimate the uncertainties that are associated with each inverted parameter and that the GS step is needed to better understand the true ambiguities that are associated with the final result.

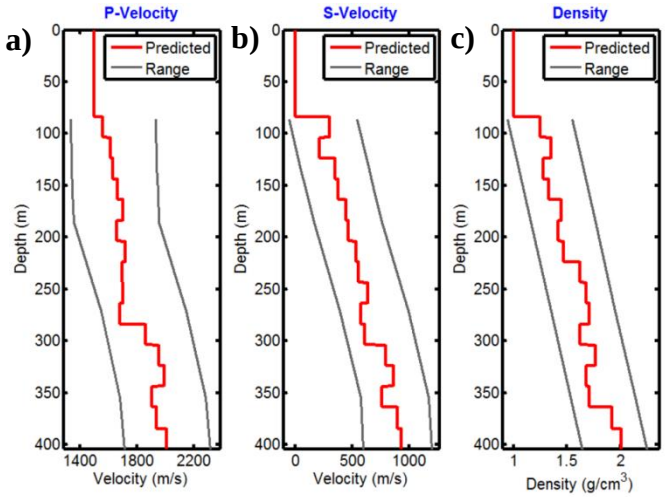

582

Figure 12: The predicted model (red lines) and the admissible ranges for each parameter (grey lines) for the P-wave velocity, S-wave velocity and density in a, b and c, respectively.

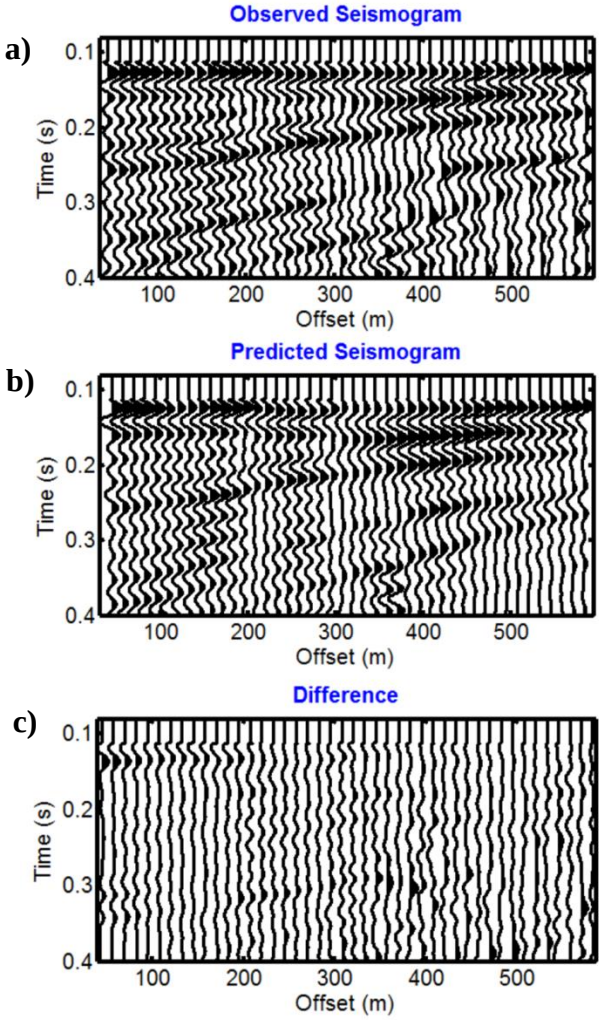

585

Figure 13: The comparison between the observed and best predicted seismogram and their difference is shown for the same frequency range during the inversion (a, b and c, respectively).

588 *The seismograms are NMO-corrected for the water velocity and are represented with the same amplitude scale.*

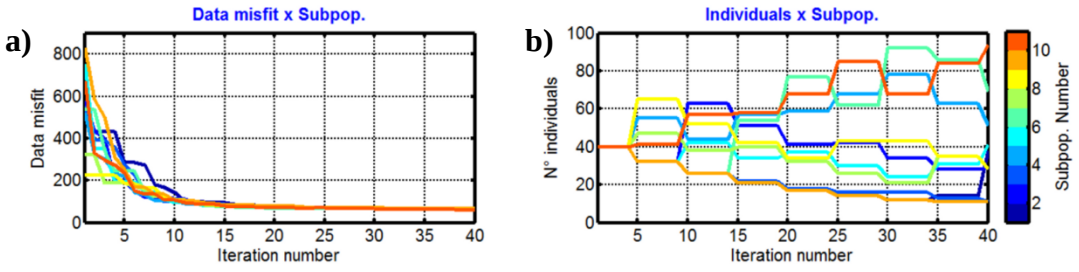

591

Figure 14: The evolution of the data misfit and the number of individuals for each subpopulation (a and b, respectively).

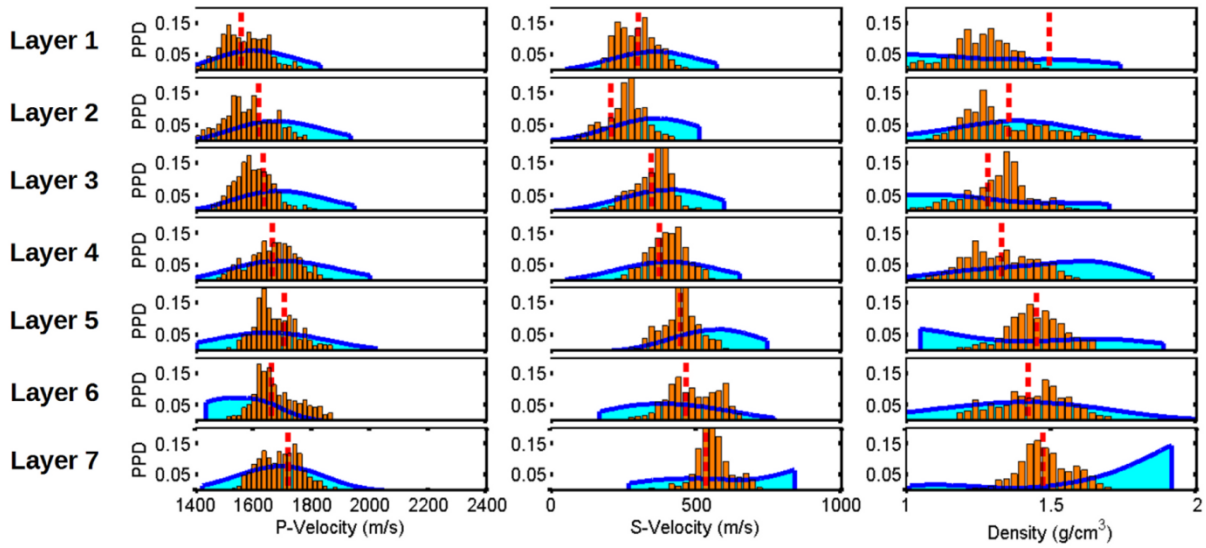

Figure 15: The GA approximation of the marginal PPDs (orange bars) and the final GA+GS estimation of the marginal distributions (cyan filled curves) are represented from top to bottom for the first seven inverted layers. The Vp, Vs and density values are represented in the left, central and right columns, respectively. The dashed red lines show the best model parameters estimated by the GA inversion. To better illustrate the variance of each parameter, the x axes are represented with the same scale.

Conclusions

We have described a hybrid method for uncertainty estimation that is applicable to stochastic inversions and combines the fast convergence of genetic algorithms with the accuracy of Gibbs sampler to estimate posterior probability distributions in model space. The first analytical test showed that the true marginal and joint distributions of the considered variables cannot be estimated from the GA models alone because the GA optimization tends to oversample the model space regions that are characterized by lower data misfit (or higher likelihood), which results in a severe underestimation of the uncertainties. A further refinement with a Gibbs sampler is needed to better estimate the uncertainties of the results and to correctly recover the correlation that exists among different inverted parameters.

Conclusions that are similar to those drawn from the analytical example can be derived from all the FWI tests on both synthetic and actual data: the validity of the hybrid GA+GS approach has been confirmed and its applicability to solving geophysical inverse problems has been positively tested. As expected, the uncertainties increase when passing from *Vp* to *Vs* and density estimations.

To avoid the overparametrization problem in the FWI inversion, we follow the approach proposed by Mallick and Dutta (2002) that fixes the layer thicknesses to a constant value of between 1/4 and 1/6 of the maximum wavelength associated with the dominant frequency. We also attempted a peculiar implementation of the niched approach to GA's to maximize the exploration of the model space and prevent the genetic drift effect. In particular, we applied different evolution strategies to different subpopulations and employed tools such as the stretching of the fitness function, shrinking of the mutation range and competition between different subpopulations. By using the data from the first synthetic example and employing the SOM clustering technique, we have demonstrated the improved model space exploration performance of our niched GA implementation compared to that of the standard, single population GA method. This advanced, niched GA inversion approach not only reduces the possibility of the genetic algorithm becoming trapped in local minima but also performs a wider exploration of the model space, which is essential to ensure a reliable estimation of the posterior probability distributions in the successive GS step.

One limitation of the GA FWI lies in the high computational cost of the stochastic optimization that, presently, makes unfeasible the applicability of the method to large, industrial scale, data volumes. However, we point out that a GA FWI is an embarrassingly parallel problem in which a large number of unrelated and independent forward problems can be solved sequentially with little or no communication among different tasks. This makes it possible for a parallel implementation to greatly speed up the inversion. In this work we used a parallel genetic algorithm implemented through a Message Passing Interface (MPI) communication protocol. This parallel implementation allowed the inversion of a single CMP gather of the field data to be completed in 6 hours, approximately. The GS algorithm is also easily parallelizable and less than half an hour was

639 required to complete this step for the field data test. These computational times refer to the use of a Octave code running on 2 compute nodes of a Linux cluster in which each compute node is a 2 esa-core Intel(R) Xeon(R) CPU E5645 at 2.4 GHz. Therefore, there is room for significant
642 improvements in the computational efficiency, for example by writing the code in a lower level language, by optimizing its parallel implementation and by running the code on many more compute nodes.

645 Another limitation of the 1D FWI is the assumption of a 1D subsurface model that limits its applicability to very simple geological contexts or to seismic data gathers that have been properly migrated (Mallick, 1999). However, despite this assumption and the high computational cost, the
648 stochastic 1D FWI is a powerful method to derive elastic models of the subsurface that can be used in many geophysical applications: e.g. well-site analysis, shallow hazard assessment (Mallick and Dutta, 2002) or reservoir characterization (Bacharach, 2006). Performing an extra Gibbs sampler
651 step adds a negligible CPU time with respect to the GA FWI and yields valuable additional information on the reliability of the estimations. Note that the uncertainties associated to the estimated elastic properties can be considered in subsequent investigations that make use of the GA
654 FWI outcomes. In this sense, they can be propagated to further estimations such as porosity or saturation estimations, to remain in a reservoir characterization context. The elastic properties estimated by 1D FWI, together with their associated posterior probability distributions, can be also
657 useful for defining different initial starting models for local, gradient-based optimizations (Xia et al. 1998). We also point out that the uncertainty and the cross-talk that affect the final estimates, as seen in our examples, particularly the *Vp*-density cross-talk and the *Vs* and density uncertainties,
660 can be greatly reduced if multicomponent seismic data or/and wide angle ranges (near or beyond the critical angle) are available (Operto et al. 2013).

As a final remark, we point out that the GA+GS method in the present implementation can not
663 be directly applied to 2D or 3D FWI due to unaffordable computational cost of the GA optimization. Currently, we are trying to extend and adapt the proposed methodology to uncertainty

quantification in 2D acoustic FWI. Our preliminary attempts indicate that it is crucial not only the availability of a highly efficient and parallel code running on tens of compute nodes, but more importantly, an efficient strategy to reduce the number of inverted model parameters in the stochastic inversion.

APPENDIX A: A brief introduction to Bayesian inference and Monte Carlo integration

The geophysical inversion problem of estimating earth model parameters from observations of geophysical data often suffers from non-uniqueness, that is several models may fit the observations equally well. Casting an inverse problem in a statistical framework (Tarantola, 2005) allows us to characterize the non-uniqueness of the solution by its probability density function (*PDF*) in model space. The main advantage of this approach lies in the fact that it produces the posterior probability density function for a model, given the observed data. Although most statistical approaches make simplistic assumptions of Gaussian prior *PDFs* and uncorrelated data errors, the results obtained from such approaches are physically meaningful and with practical utility. In this section, we give a brief overview of the Bayesian formulation, following the concepts described in Sen and Stoffa (1996).

As usual, we represent the model by a vector m and the data by a vector d given by:

$$m = [m_1, m_2, \ldots, m_M]^T \qquad (A1)$$

and

$$d = [d_1, d_2, \ldots, d_N]^T \qquad (A2)$$

consisting of elements m_i and d_i, respectively, where each element is considered to be a random variable. The quantities M and N are the number of model parameters and data points, respectively, and the superscript T represents a matrix transpose. Following Tarantola (2005) notation, we assume that $p(d|m)$ is the *PDF* of d for a given m (also called the likelihood function), $p(m|d)$ is the conditional *PDF* of m for a given d, $p(d)$ is the *PDF* of data set d and $p(m)$ is the *PDF* of model m independent of the data. From the definition of the conditional probabilities, we have:

$$p(m \mid d)\, p(d) = p(d \mid m)\, p(m) \qquad (A3)$$

From this formulation we obtain an equation for the conditional *PDF* of model m given the measured data d as follows:

$$p(m \mid d) = \frac{p(d \mid m)\, p(m)}{p(d)} \qquad (A4)$$

696 which describes the state of information for model *m* given the data *d*. This equation is the so-called Bayes' rule. The denominator *p*(*d*) does not depend on *m* and can be considered a constant factor in the inverse problem (Duijndam, 1988). Replacing the denominator in equation with a
699 constant, we have:

$$p(m \mid d) \propto p(d \mid m)\, p(m) \qquad (A5)$$

The *PDF p*(*m*) is the probability of the model *m*, independent of the data, i.e. it describes the
702 information for the model without any knowledge of the data and is called the prior *PDF*. Similarly, the *PDF p(m|d)* is the state of information on model *m* given the data and is called the posterior *PDF* or the PPD. Obviously, the prior knowledge in the model is modified by the likelihood
705 function, but assuming a uniform prior *PDF*, the posterior *PDF* is primarily determined by the likelihood function (Duijndam, 1988). Assuming Gaussian errors (Sen and Stoffa, 1996), the likelihood function takes the following form:

708 $$p(d \mid m) \propto \exp\left[-E(m)\right] \qquad (A6)$$

where *E(m)* is a misfit function that we want to minimize in the inversion process. The expression for the PPD can thus be written as

711 $$p(m \mid d) \propto \exp\left[-E(m)\right] p(m) \qquad (A7)$$

This PPD is the final solution of the inversion problem from a Bayesian point of view. However, the PPD can not be displayed in a multi-dimensional space. Therefore, several measures of
714 dispersion and marginal density functions can be used to describe the solution. Among these, the marginal PPD of a particular model parameter, the mean model and the posterior model covariance matrix are, respectively, given by:

717 $$p(m_i \mid d) = \int dm_1 \int dm_2 \ldots \int dm_{i-1} \int dm_{i+1} \ldots \int dm_M \; p(m \mid d) \qquad (A8)$$

$$\overline{m} = \int dm \; m \; p(m \mid d) \qquad (A9)$$

and

$$C_M = \int dm\,(m-\overline{m})(m-\overline{m})^T\, p(m\,|\,d) \qquad (A10)$$

Equations *A8-A10* are often referred to as the Bayesian integrals and, for a non-linear inverse problem, they can be calculated via a numerical evaluation (see Sen and Stoffa, 1996; Sambridge, 1999). The generic Bayesian integral *I*, can be expressed as:

$$I = \int dm\; f(m)\, P(m) \qquad (A11)$$

where the domain of integration spans the entire model space and *f(m)* represents a generic function used to define each integrand. To simplify the notation, in equation *A11* we substitute *p(m|d)* with *P(m)* dropping the *|d* term. We maintain this notational simplification from here on.

Using a Monte Carlo integration technique, a numerical approximation of equation *A11* can be derived as follows:

$$\overline{I} = \frac{1}{N}\sum_{k=1}^{N}\frac{f(m_k)P(m_k)}{q(m_k)} \qquad (A12)$$

where $\overline{I}$ indicates the numerical approximation of the Bayesian integrals, *N* is the number of Monte Carlo integration points and *q(m)* is their density distribution that is assumed to be normalized:

$$\int dm\, q(m) = 1 \qquad (A13)$$

Equation *A12* can be finally re-written as a simple weighted average over the ensemble of Monte Carlo integration points:

$$\overline{I} = \frac{1}{N}\sum_{k=1}^{N} f(m_k)w_k \qquad (A14)$$

where w_k indicates the frequently called “important ratio” and is equal to:

$$w_k = \frac{P(m_k)}{q(m_k)} \qquad (A15)$$

741

APPENDIX B: Using the Gibbs sampler to approximate the Bayesian integrals

In the following we give a brief description of the GS step that constitutes the second part of the
744 proposed methodology. We refer the reader to Sambridge (1999) for more detailed mathematical information.

The GS algorithm exploits the finite ensemble of models collected during the GA optimization,
747 and their associate likelihood, to refine the PPD estimated by the GA method. This can be viewed as an interpolation problem in a multi-dimensional space (Sambridge, 1999). After performing a GA inversion, in which all the explored models and associated likelihoods have been saved and
750 stored, the GA approximation of the PPD can be derived by constructing a multi-dimensional interpolant using Voronoi cells in the model space (Voronoi 1908). This approximate PPD is derived by simply setting the known PPD of each model as a constant inside its Voronoi cell. We
753 call this the GA approximation of the PPD, and write it as

$$P_{GA}(m) = P(m_i^{GA}) \qquad (B1)$$

where m_i^{GA} is a model in the input ensemble of GA-sampled models that is closest to m (a
756 generic point in the model space). In particular, $P_{GA}(m)$ represents all information contained in the input ensemble and constitutes the only information available in the GS step to compute the final PPD. If we assume an efficient exploration of the model space during the GA optimization, we can
759 consider $P_{GA}(m)$ as a rough approximation of the target, final, PPD $P(m)$. Then, we have:

$$P_{GA}(m) \approx P(m) \qquad (B2)$$

This final PPD can be computed using a MCMC algorithm (such as the Gibbs sampler) that
762 generates a new set of Monte Carlo samples (that will constitute the resampled ensemble) the distribution of which asymptotically tends towards $P_{\mathrm{GA}}(m)$. In other words, the new samples drawn during the GS walk are designed to importance sample the GA approximation of the PPD. The
765 rejection method (Gilks and Wild, 1992) can be used to generate such resampled ensemble.

During the GS walks the density distribution of the resampled ensemble (indicated with *q(m)* in equation *A12*) satisfies the following relation:

$$q(m) \approx P_{GA}(m) \qquad (B3)$$

The assumption that the $P_{GA}(m)$ is a rough approximation of the target *P(m)* (see equation *B2*) determines that the importance ratio (indicated with *w* in equation A14) can be approximated to 1 according to the following equation:

$$w = \frac{P(m)}{P_{GA}(m)} \approx 1 \qquad (B4)$$

Then, the Bayesian integral of equation *A12* becomes a simple average over the resampled ensemble:

$$\bar{I} = \frac{1}{N} \sum_{k=1}^{N} f(m_k^{GS}) \qquad (B5)$$

where m_k^{GS} is a generic model sampled by the GS algorithm, *N* is the total number of resampled points and *f* is the generic function already introduced in equation *A11*.

The computational time (*t*) of the GS step linearly depends on the number of GS walks (*Ns*), on the number of models drawn per walk (*Nr*) and on the dimension of the model space (*d*) according to the following expression:

$$t \propto Nr\ Ns\ d \qquad (B6)$$

As suggested by Sambridge (1999) it is advisable that *Nr>>Ns*. In addition it is also preferable to use multiple independent random walks (*Ns>1*), each starting from different point in model space. The value of *Nr* and *Ns* should increase with the dimension of the models space and with the dimension of the input ensemble. Higher *Ns* and *Nr* values ensure more reliable approximations of the Bayesian integrals, although increasing the computational time. The convergence of the GS algorithm to a stable posterior distribution can be checked by computing the Potential Scale Reduction (PSR) factor (Gelman et al. 2013). This number quantifies the difference between the "within-walk" and "between-walk" estimated variances. The PSR factor decreases to 1 as the

number of drawn samples (*N*) tends to infinite. A high PSR value indicates that the variance within the walks is small compared to that between the walks and that longer walks are needed to converge
792 to a stable distribution. Usually, a PSR factor lower than 1.2 for a given unknown proves that convergence has been achieved for that particular model parameter. Based on our experience of GS applications in the context of 1D elastic FWI, we note that convergence of the GS is usually
795 obtained when *Nr* is 30-40 times the number of unknowns, whereas a *Ns* value between 70 and 100 is usually adequate. Obviously, the optimal *Nr* and *Ns* values depend not only on the number of unknowns but also on the topography of the misfit function. For example, the convergence of the
798 algorithm can be more problematic in case of many local minima or in case of a severely ill-conditioned inverse problem with a nearly flat misfit function.

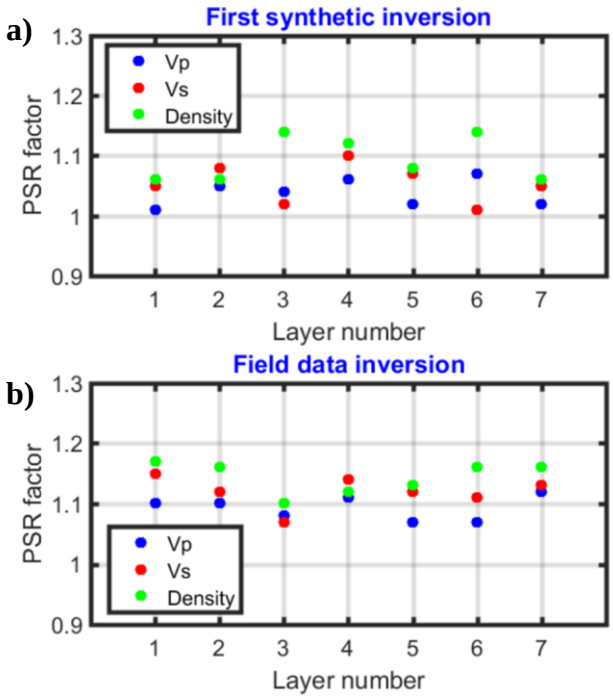

801 *Figure 16: a) and b) Examples of PSR factor values for the first synthetic inversion and for the field data inversion, respectively.*

804 Figures 16a and 16b show the PSR values for the *Vp*, *Vs* and density in the first seven layers, that are the layers which PPDs have been analyzed in the paper, for the first synthetic test and the field data example, respectively. The PSR values for the second synthetic test are very similar to those of

the first test and thus are not shown. Note that for both cases the PSR values for all the variables in every layer are below 1.2 indicating that GS has attained the desired convergence. Note also that the PSR factor tends to increase moving from the synthetic inversion to the field data inversion and from *Vp* to *Vs* to density. These increases indicate that the convergence of the GS algorithm is, as expected, slightly more problematic for the density (the less resolvable parameter) and for the field data inversion.

Acknowledgements

We wish to thank two unknown reviewers and an AE for their acute questions and constructive comments that helped to improve the paper.

References

- Aki K. and Richards P. G. 1980: Quantitative seismology: Theory and methods. WH Freeman and Co.
- Bäck, T., and Hoffmeister, F. 1991. Extended selection mechanisms in genetic algorithms. Morgan Kaufmann publisher.
- Bachrach, R. 2006. Joint estimation of porosity and saturation using stochastic rock-physics modeling. Geophysics, 71(5), O53-O63.
- Backus, G. E. 1962. Long-wave elastic anisotropy produced by horizontal layering. Journal of Geophysical Research, **67**(11), 4427-4440.
- Bellman, R. E., 1957. Dynamic programming: Princeton University Press.
- Blickle, T., and Thiele, L. 1995. A comparison of selection schemes used in genetic algorithms. TIK report, 11.
- Datta, D., 2015. Estimating Starting Models for Full Waveform Inversion Using a Global Optimization Method. 77th EAGE Conference and Exhibition.
- Diouane, Y., Calandra, H., Gratton, S., and Vasseur, X. 2014. A Parallel Evolution Strategy for Acoustic Full-Waveform Inversion. In EAGE Workshop on High Performance Computing for Upstream. DOI: 10.3997/2214-4609.20141923.
- Duijndam, A. J. W. 1988. Bayesian Estimation in Seismic Inversion. Part 1: PRINCIPLES. Geophysical Prospecting, **36**(8), 878-898.
- Evensen, G. 2009. Data assimilation: the ensemble Kalman filter. Springer Science & Business Media.
- Fliedner, M. M., Treitel, S., and MacGregor, L. 2012. Full-waveform inversion of seismic data with the Neighborhood Algorithm. The Leading Edge, **31**(5), 570-579.
- Gao, Z., J. Gao, P. Zhibin, and X. Zhang, 2014. Building an initial model for full waveform inversion using a global optimization scheme. SEG Technical Program Expanded Abstracts, 1136-1141.

846 • Geman, S., and Geman, D. 1984. Stochastic relaxation, Gibbs distributions, and the Bayesian restoration of images. Pattern Analysis and Machine Intelligence, IEEE Transactions on, **6**, 721-741.

849 • Gelman, A., Carlin, J. B., Stern, H. S., Dunson, D. B., Vehtari, A., and Rubin, D. B. 2013. Bayesian data analysis. CRC press.

• Gilks, W. R., and Wild, P. 1992. Adaptive rejection sampling for Gibbs sampling. Applied 852 Statistics, 337-348.

• Goldberg, D. E., and Segrest, P. 1987. Finite Markov chain analysis of genetic algorithms. In Proceedings of international conference on genetic algorithms, 1.

855 • Goldberg, D. E. 1989. Genetic algorithms in search, optimization, and machine learning. Reading Menlo Park: Addison-wesley.

• Goldberg, D. E., and Deb, K. 1991. A comparative analysis of selection schemes used in 858 genetic algorithms. Urbana, **51**, 61801-2996.

• Gould, S. J., and Eldredge, N. 1977. Punctuated equilibria: the tempo and mode of evolution reconsidered. Paleobiology, 115-151.

861 • Gouveia, W. P., and Scales, J. A. 1997. Resolution of seismic waveform inversion: Bayes versus Occam. Inverse problems, 13(2), 323.

• Gouveia, W. P., and Scales, J. A. 1998. Bayesian seismic waveform inversion: Parameter 864 estimation and uncertainty analysis. Journal of Geophysical Research: Solid Earth, 103(B2), 2759-2779.

• Holland, J. H. 1975. Adaptation in natural and artificial systems: An introductory analysis 867 with applications to biology, control, and artificial intelligence. University Michigan Press.

• Hong, T., and Sen, M. K. 2009. A new MCMC algorithm for seismic waveform inversion and corresponding uncertainty analysis. Geophysical Journal International, **177**(1), 14-32.

870 • Horn, J. 1993. Finite Markov chain analysis of genetic algorithms with niching. Forrest, **727**, 110-117.

- Jin, L., Sen, M.K., and Stoffa, P.L. 2008. One-dimensional prestack seismic waveform inversion using Ensemble Kalman Filter. SEG Technical Program Expanded Abstracts 2008, 1920-1924.
- Kennett, B. L. 1983. Seismic wave propagation in stratified media. Cambridge University Press.
- Li, T., and Mallick, S. 2015. Multicomponent, multi-azimuth pre-stack seismic waveform inversion for azimuthally anisotropic media using a parallel and computationally efficient non-dominated sorting genetic algorithm. Geophysical Journal International, 200(2), 1134-1152.
- Mallick, S. 1999. Some practical aspects of prestack waveform inversion using a genetic algorithm: An example from the east Texas Woodbine gas sand. Geophysics, 64(2), 326-336.
- Mallick, S., and Dutta, N. C. 2002. Shallow water flow prediction using prestack waveform inversion of conventional 3D seismic data and rock modeling. The Leading Edge, **21**(7), 675-680.
- Mallick, S., Mukhopadhyay, P.K., Padhi A., and Alvarado V. 2010. Prestack Waveform Inversion- the present state and the road ahead. SEG Technical Program Expanded Abstracts 2010, 4428-4431.
- de Matos, M. C., Osorio, P. L., and Johann, P. R. 2006. Unsupervised seismic facies analysis using wavelet transform and self-organizing maps. Geophysics, 72(1), P9-P21.
- Mitchell, M. 1998. An introduction to genetic algorithms. MIT press.
- Morgan, J., Warner, M., Bell, R., Ashley, J., Barnes, D., Little, R., Roele, K. and Jones, C. 2013. Next-generation seismic experiments: wide-angle, multi-azimuth, three-dimensional, full-waveform inversion. Geophysical Journal International, **195**(3), 1657-1678.
- Operto, S., Gholami, Y., Prieux, V., Ribodetti, A., Brossier, R., Metivier, L., and Virieux, J. (2013). A guided tour of multiparameter full-waveform inversion with multicomponent data: From theory to practice. The Leading Edge, 32(9), 1040-1054.
- Schlierkamp-Voosen, D. and Mühlenbein, H., 1993. Predictive models for the breeder genetic algorithm. Evolutionary computation, **1**(1), 25-49.

- Prieux, V., Brossier, R., Gholami, Y., Operto, S., Virieux, J., Barkved, O. and Kommedal, J. 2011. On the footprint of anisotropy on isotropic full waveform inversion: The Valhall Case Study. Geophysical Journal International, **187**, 1495–1515.
- Reeves, C. R., and J. E. Rowe, 2002. Genetic Algorithms - Principles and Perspectives (A guide to GA Theory). Kluwer Academic Publisher.
- Rubinstein, R. Y., and Kroese, D. P. 2011. Simulation and the Monte Carlo method. John Wiley & Sons.
- Sambridge, M. 1999. Geophysical inversion with a neighbourhood algorithm—II. Appraising the ensemble. Geophysical Journal International, **138**(3), 727-746.
- Sajeva, A., Aleardi, M., Mazzotti, A., Bienati, N., and Stucchi E. 2014a. Estimation of velocity macro-models using stochastic full-waveform inversion. SEG Technical Program Expanded Abstracts 2014, 1227-1231. doi: 10.1190/segam2014-1088.1
- Sajeva, A., Aleardi, M., Mazzotti, A., Stucchi, E., and Galuzzi, B. 2014b. Comparison of Stochastic Optimization Methods on Two Analytic Objective Functions and on a 1D Elastic FWI. In 76th EAGE Conference and Exhibition 2014. doi: 10.3997/2214-4609.20140857
- Schlierkamp-Voosen, D., and Mühlenbein, H. 1996. Adaptation of population sizes by competing subpopulations. In Proceedings of the 1996 IEEE Conference on Evolutionary Computation.
- Sen, M. K., and Stoffa, P. L. 1991. Nonlinear one-dimensional seismic waveform inversion using simulated annealing. Geophysics, **56**(10), 1624-1638.
- Sen, M. K., and Stoffa, P. L. 1992. Rapid sampling of model space using genetic algorithms: examples from seismic waveform inversion. Geophysical Journal International, **108**(1), 281-292.
- Sen, M. K., and Stoffa, P. L. 1996. Bayesian inference, Gibbs' sampler and uncertainty estimation in geophysical inversion. Geophysical Prospecting, **44**(2), 313-350.
- Sirgue, L., Barkved, O. I., Dellinger, J., Etgen, J., Albertin, U. and Kommedal, J. H. 2010 Full waveform inversion: The next leap forward in imaging at Valhall. First Break, **28**, 65–70.

924 • Sivanandam, S. N., and Deepa, S. N. 2008. Genetic Algorithm Optimization Problems. Springer Berlin Heidelberg.

• Tanese, R. 1987. Parallel genetic algorithm for a hypercube. In Proceedings of international 927 conference on genetic algorithms, 177-183.

• Tarantola, A. 1986. A strategy for nonlinear elastic inversion of seismic reflection data. Geophysics, 51(10), 1893-1903.

930 • Tarantola, A. 2005. Inverse problem theory and methods for model parameter estimation. Siam.

• Tognarelli A., Stucchi, E.M., Bienati, N., Sajeva, A., Aleardi, M., and Mazzotti, A. 2015. 933 Two grid stochastic Full Waveform Inversion of 2D Marine Seismic Data. In 77th EAGE Conference and Exhibition 2015.

• Ultsch, A. 1993. Self-organizing neural networks for visualisation and classification. 936 Springer Berlin Heidelberg.

• Virieux, J. and Operto, S. 2009. An overview of full-waveform inversion in exploration geophysics. Geophysics, **74**, 6, WCC1-WCC26.

939 • Voronoi, G. 1908. Nouvelles applications des paramètres continus à la théorie des formes quadratiques. Premier mémoire. Sur quelques propriétés des formes quadratiques positives parfaites. Journal für die reine und angewandte Mathematik, 133, 97-178.

942 • Xia, G., Sen, M. K., and Stoffa, P. L. 1998. 1-D elastic waveform inversion: A divide-and-conquer approach. Geophysics, 63(5), 1670-1684.

945

Figures and Captions

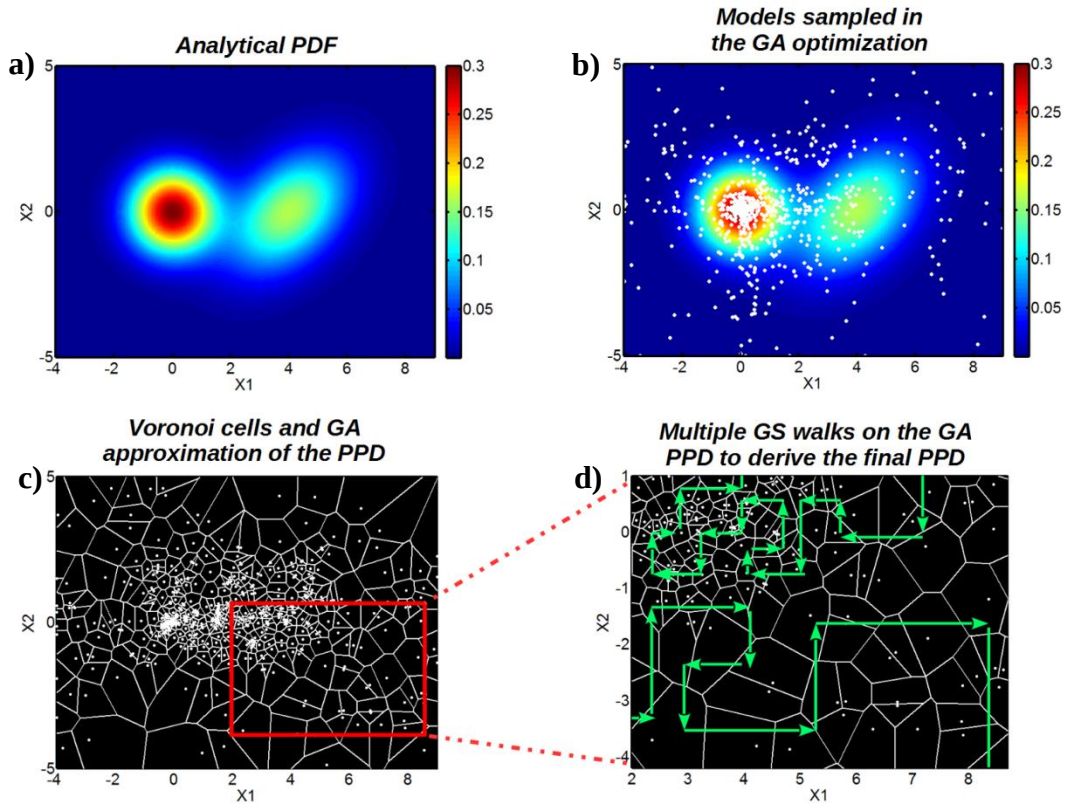

948 *Figure 1: Examples of the different steps that characterize the hybrid GA+GS approach. a) The initial analytical PDF that was used in the optimization. b) The 1000 models (white dots) that were sampled during the GA optimization. c) The model space portion that is explored during the GA* 951 *step is divided into Voronoi cells (delimited by the white lines), and the likelihood that is associated with each explored model is assigned to the entire cell. This step results in the GA approximation of the PPD. d) Multiple GS walks (examples of GS walks are illustrated by the green paths) are used* 954 *to draw samples from the GA approximation of the PPD. This step gives the final PPD that was estimated by the GA+GS approach.*

957

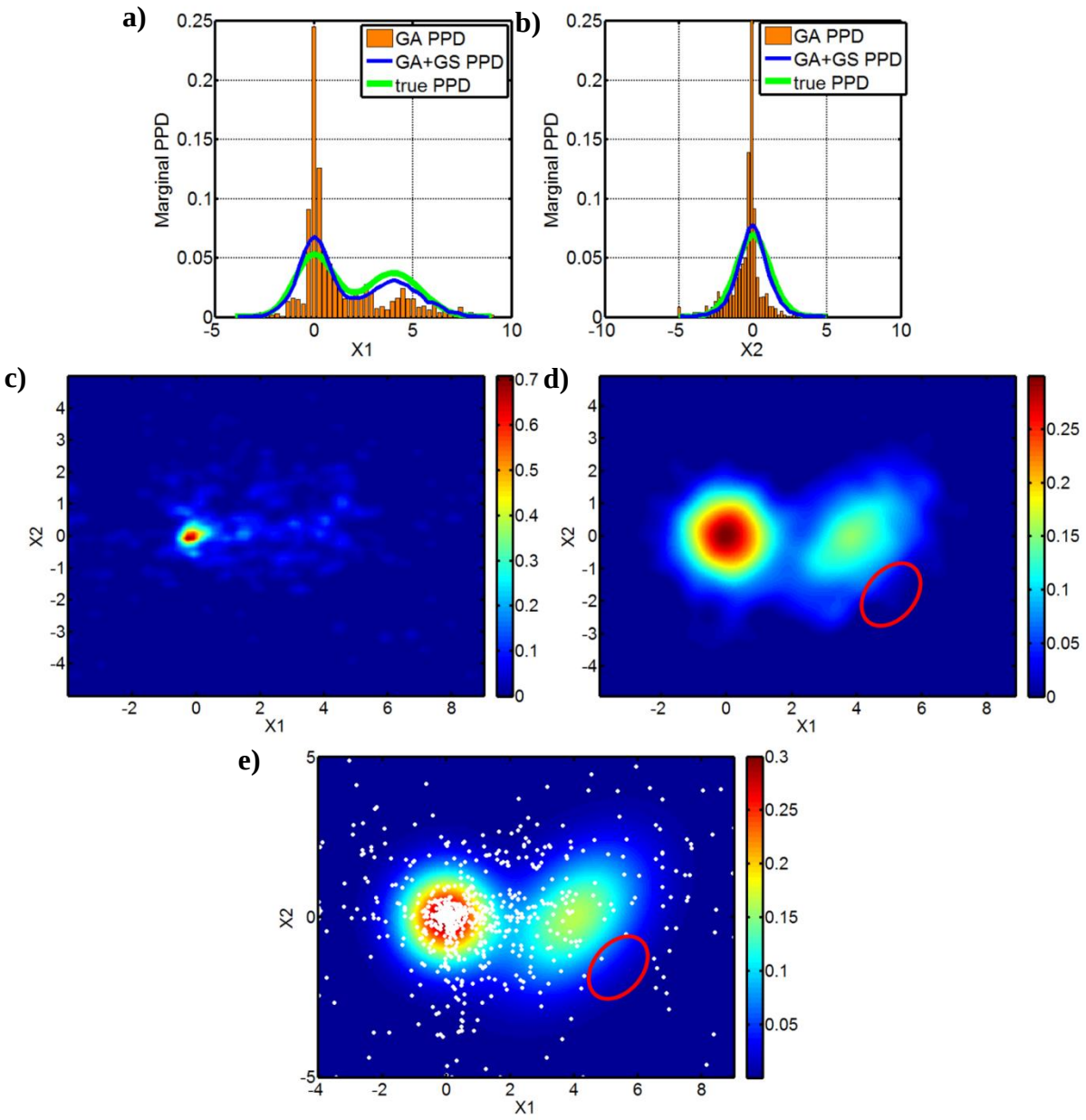

960 *Figure 2: In a) and b), comparisons are shown for the variables x_1 and x_2 from the true marginal distributions (green lines), the marginal PPDs that were estimated by the GA method (orange bars) and the GA+GS marginal PPD estimations (blue lines). c) The GA approximation of the joint* 963 *distribution. Note the strong underestimation of the uncertainties that resulted from the oversampling of the model space region with the highest probability. d) The final joint PPD that was estimated by the GA+GS method (compare with the true joint probability distribution that is* 966 *shown in e) and the GA joint estimation that is shown in c)). Note the different colour-scale in c)*

and d). e) The true joint posterior distribution (in colour) that is defined by equation 1 and represented in Figure 1a. The white dots represent the 1000 models that were sampled in the GA optimization. The red circle in d) and e) marks the area where the differences between the true and estimated GA+GS joint PPDs are more prominent. See the text for additional comments.

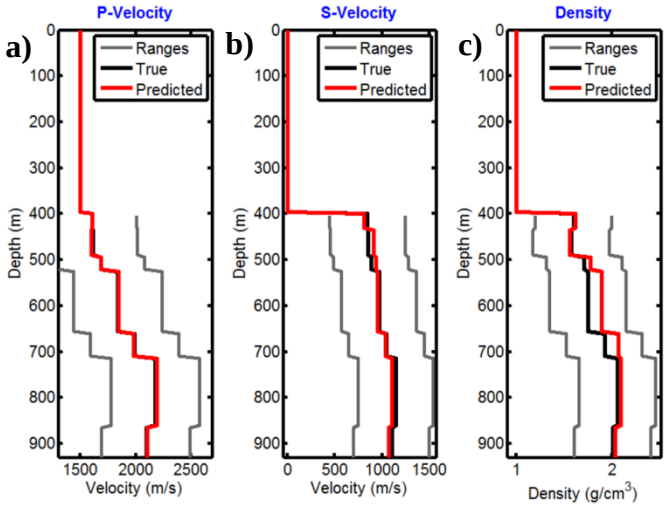

Figure 3: Comparison between the true (black) and predicted (red) elastic properties (a, b and c for Vp, Vs and density, respectively). The grey lines show the parameter ranges that were used during the inversion.

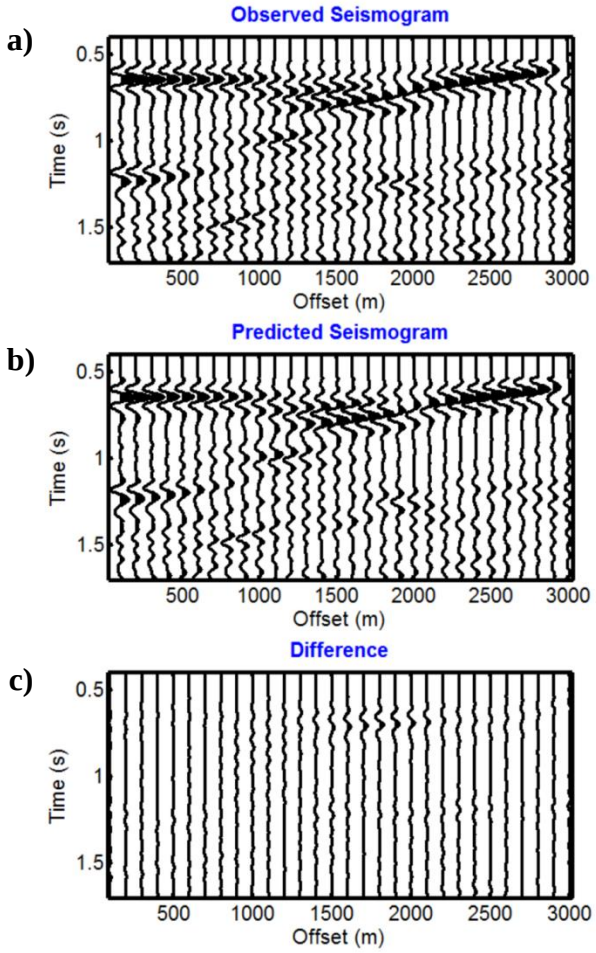

981 *Figure 4: a) Observed seismogram, b) best predicted seismogram and c) their difference. The seismograms are NMO-corrected for the water velocity and are represented with the same amplitude scale.*

984

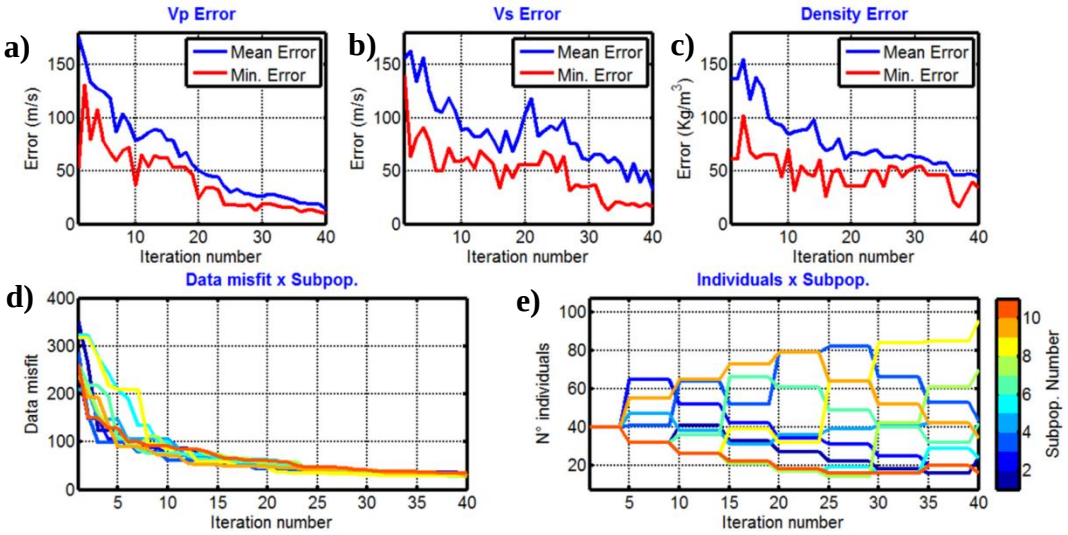

987 *Figure 5: Evolution of the mean and the best model misfit for the Vp, Vs and density parameters as a function of iteration number (a, b and c, respectively). Evolution of the data misfit (d) and the number of individuals (e) for each subpopulation.*

990

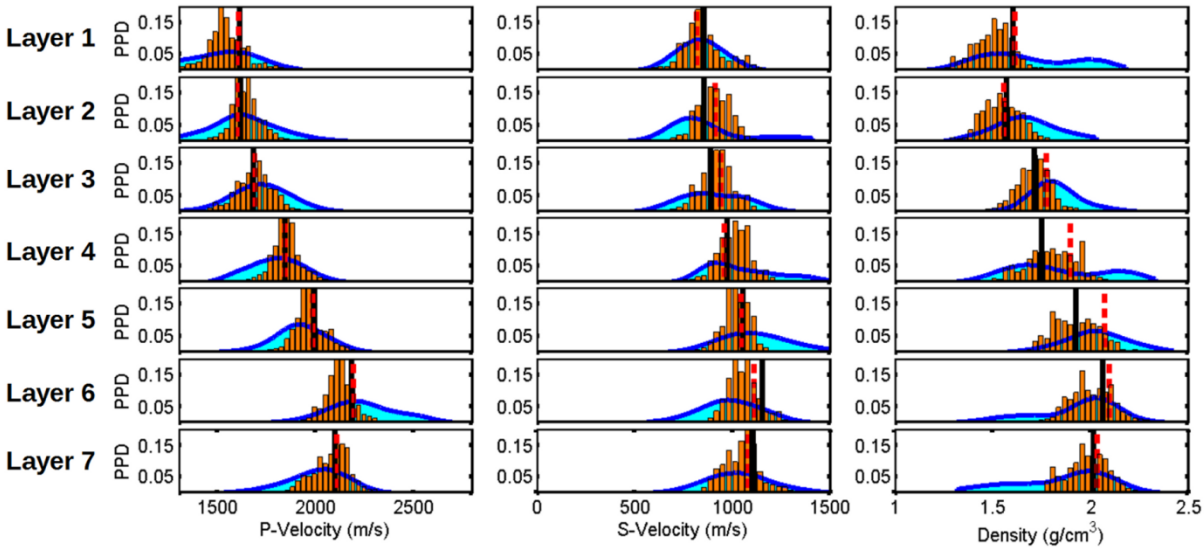

993 *Figure 6: The GA approximation of the marginal PPDs (orange bars) and the final GA+GS estimation of the marginal distributions (cyan filled blue curves) are displayed from top to bottom for each inverted layer. The Vp, Vs and density values are represented in the left, central and right* 996 *columns, respectively. The continuous black and dashed red lines illustrate the true and the predicted model parameters by the GA inversion, respectively. To better display the variance of each parameter, the x axes are represented with the same scale.*

999

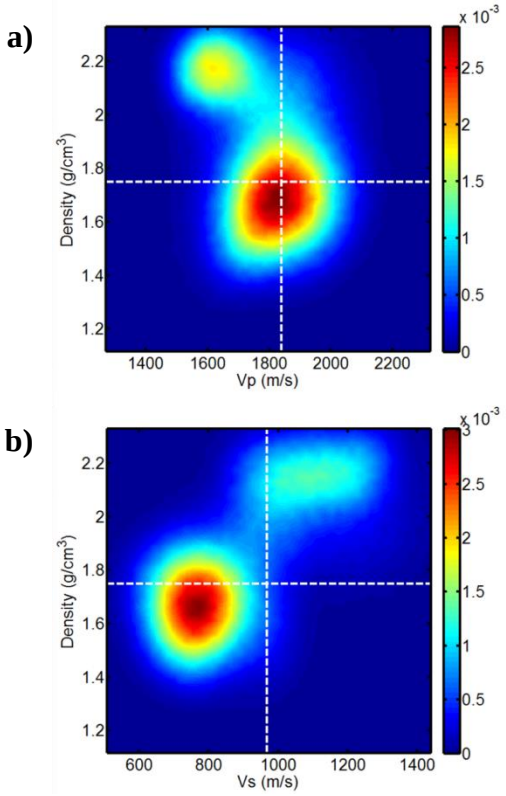

Figure 7: The posterior 2D marginal distributions for the fourth layer. The Vp-density and Vs-density joint distributions are shown in a) and b), respectively. The dotted white lines represent the true values. To better compare the resolution that is associated with each parameter, the axes are represented with the same scale.

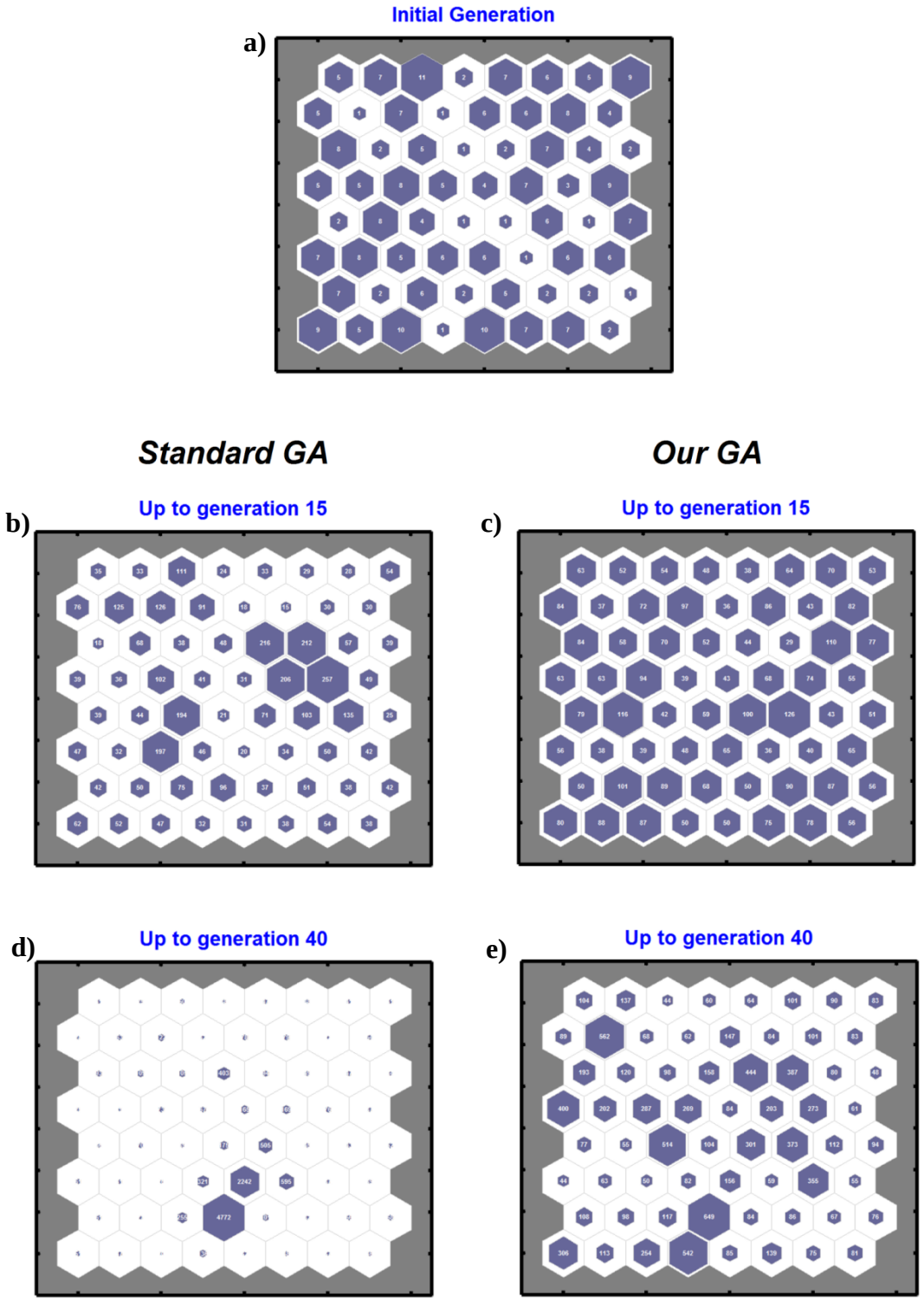

Figure 8: Sample hits plots that represent the different evolutions of the standard single-population and our GA implementation. Each plot is generated by clustering the entire set of generated models up to a certain generation and projecting the result to a two-dimensional map

(see the text for more details). The two tests start from the initial, randomly generated population of models (a). The evolution of the standard single-population GA case is represented in b) and d),
1017 *whereas c) and e) represent the evolution of our GA inversion. This figure demonstrates that the proposed GA implementation is characterized by a wider exploration of the model space compared with the standard GA.*

1020

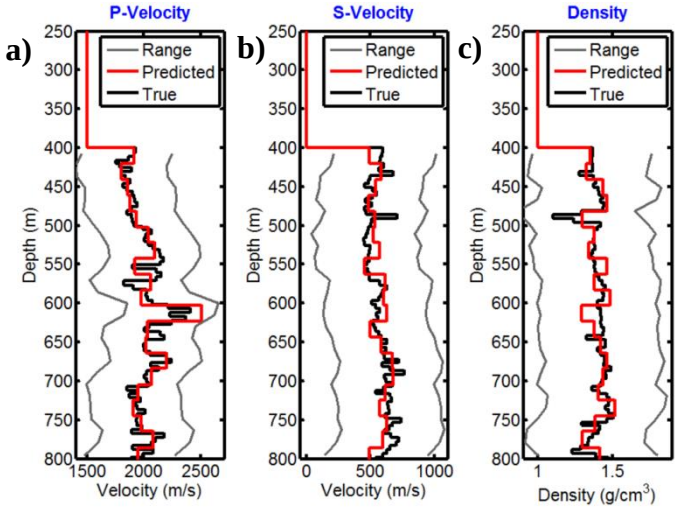

1023 *Figure 9: Comparison between the true (black) and the predicted (red) elastic properties (a, b and c). The black curves represent the log data after Backus averaging for a dominant frequency of 50 Hz. The red curves indicate the predicted elastic properties for a dominant frequency of 15 Hz.* 1026 *The grey lines show the inversion parameter ranges that have been defined around a highly smoothed version of the original log data.*

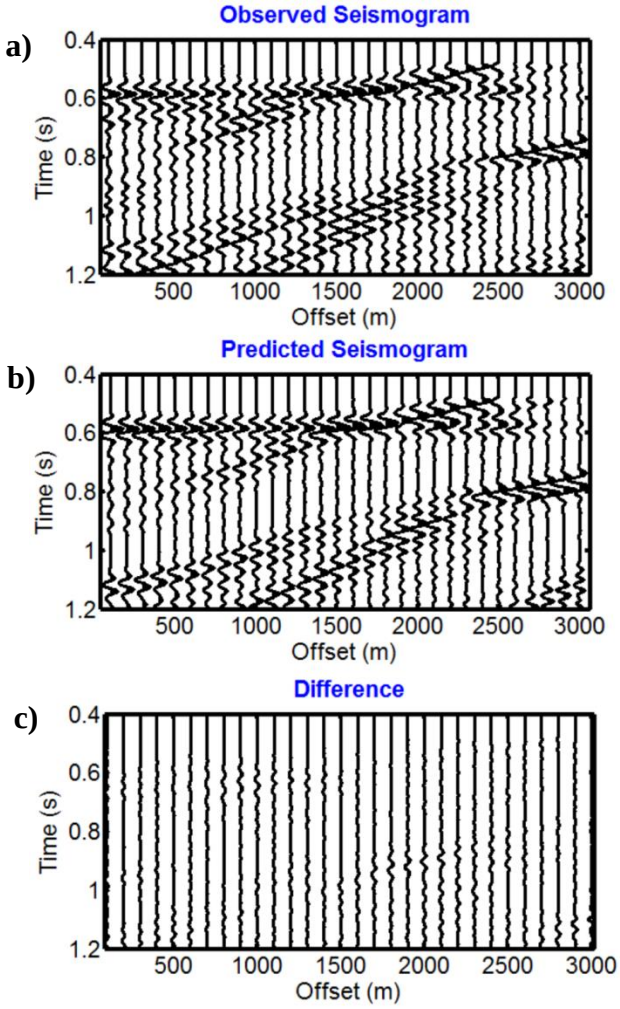

Figure 10: a) Observed seismogram, b) best predicted seismogram and c) their difference for the same frequency range during the inversion (which determines the layer thickness of the inverted model). The seismograms are NMO-corrected for the water velocity and are represented with the same amplitude scale.

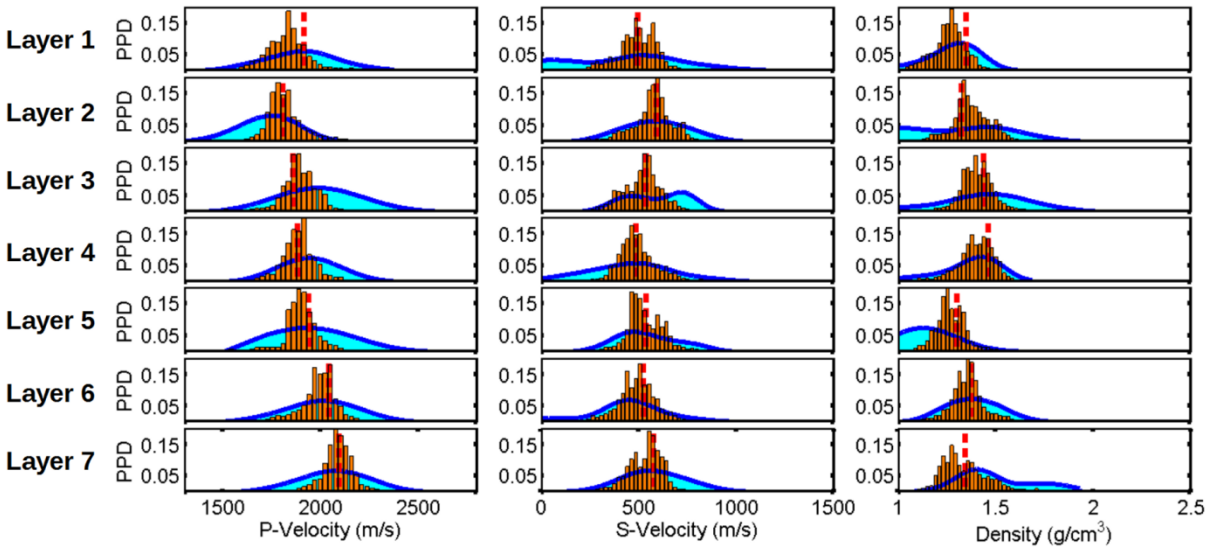

Figure 11: The GA approximation of the marginal PPDs (orange bars) and the final GA+GS estimation of the marginal distributions (cyan filled curves) are shown from top to bottom for the first seven layers. The Vp, Vs and density values are represented in the left, central and right columns, respectively. The dashed red lines show the predicted model parameters by the GA inversion. To better display the variance of each parameter, the x axes are represented with the same scale.

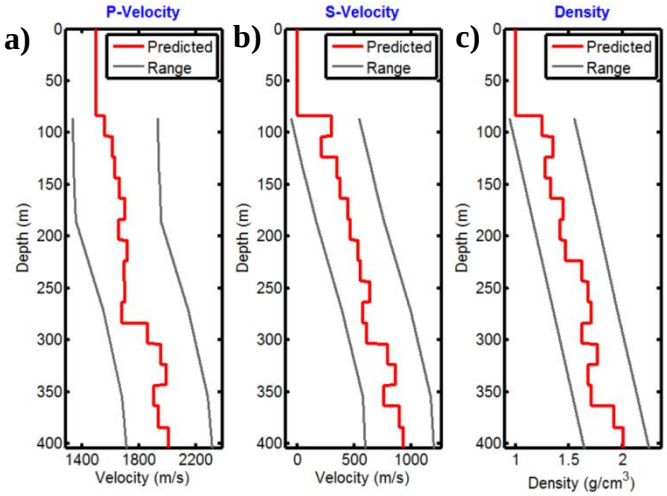

1047

Figure 12: The predicted model (red lines) and the admissible ranges for each parameter (grey lines) for the P-wave velocity, S-wave velocity and density in a, b and c, respectively.

1050

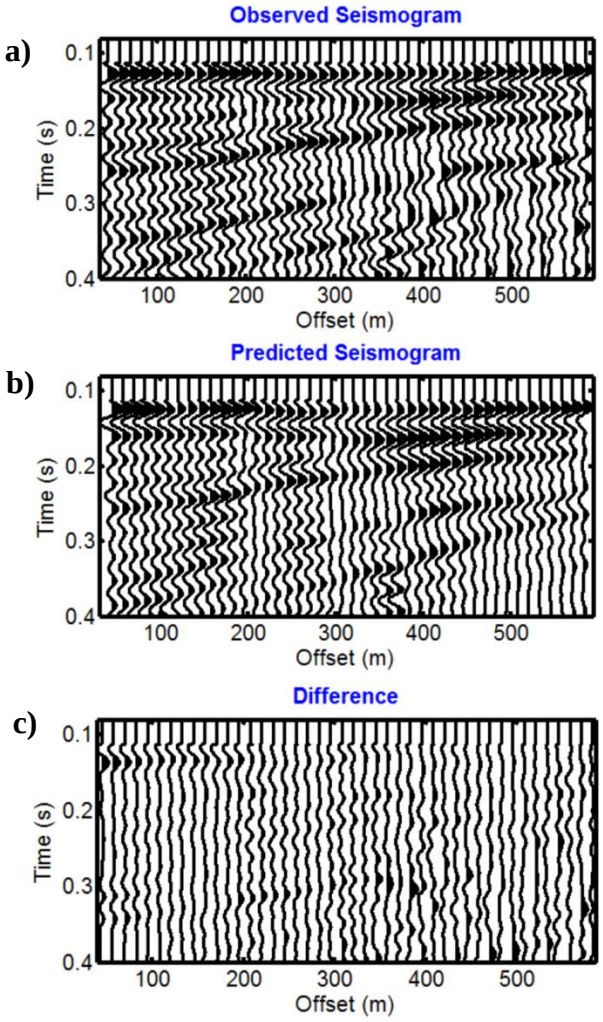

Figure 13: The comparison between the observed and best predicted seismogram and their difference is shown for the same frequency range during the inversion (a, b and c, respectively). The seismograms are NMO-corrected for the water velocity and are represented with the same amplitude scale.

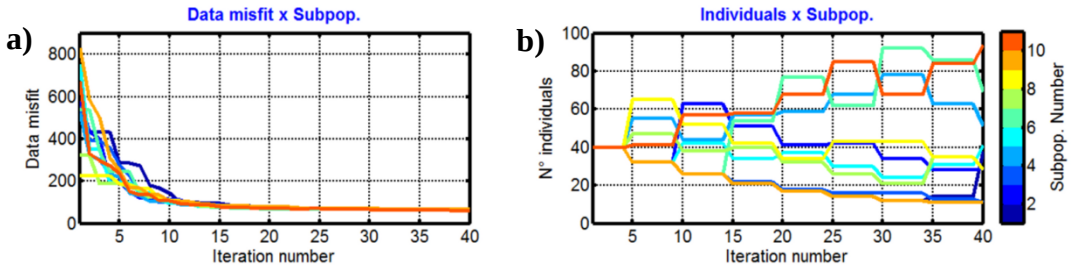

Figure 14: The evolution of the data misfit and the number of individuals for each subpopulation (a and b, respectively).

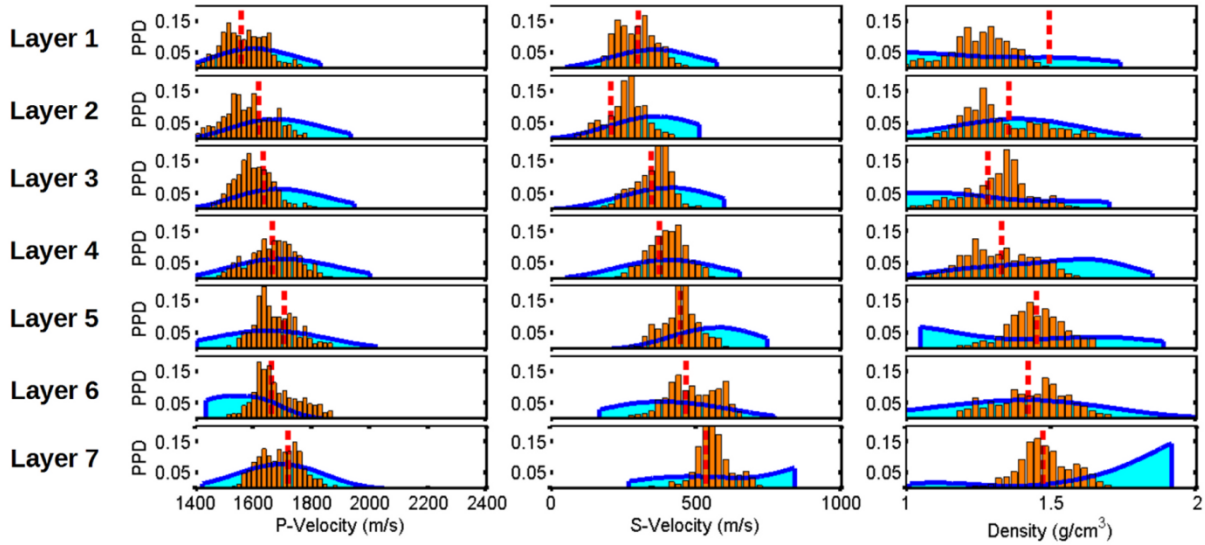

Figure 15: The GA approximation of the marginal PPDs (orange bars) and the final GA+GS estimation of the marginal distributions (cyan filled curves) are represented from top to bottom for the first seven inverted layers. The Vp, Vs and density values are represented in the left, central and right columns, respectively. The dashed red lines show the best model parameters estimated by the GA inversion. To better illustrate the variance of each parameter, the x axes are represented with the same scale.

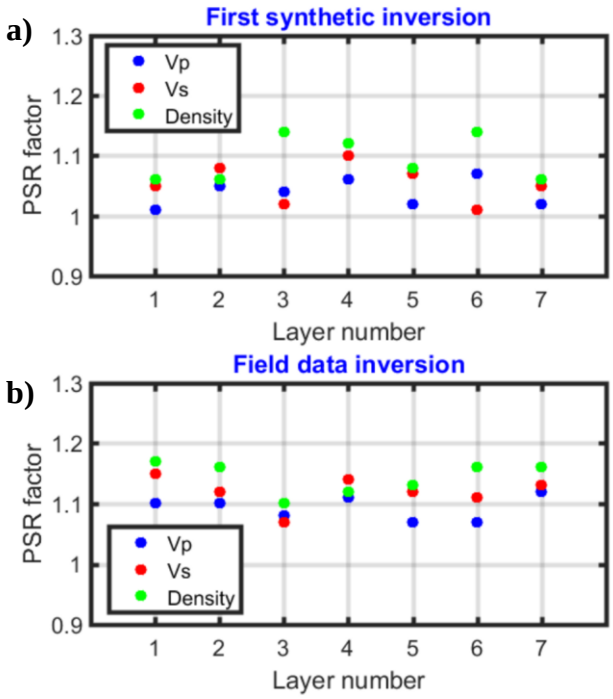

1074 *Figure 16: a) and b) Examples of PSR factor values for the first synthetic inversion and for the field data inversion, respectively.*

1077